

APPROCHE MULTI-ÉCHELLE DE LA  
FORMATION ET L'ÉVOLUTION DES AMAS  
D'ÉTOILE

Julien Dorval

A thesis submitted for the degree of Doctor of  
Philosophy

May 2014



# Contents

Historical foreword: from Aristotle to GPU computing . . . . .	1
<b>1 Introduction</b>	<b>9</b>
1.1 Introduction to star clusters . . . . .	10
1.1.1 Why study them ? . . . . .	10
1.1.2 Types of star clusters . . . . .	11
1.2 Some important dynamical concepts . . . . .	13
1.2.1 Virial theorem . . . . .	13
1.2.2 Dynamical timescales . . . . .	13
1.2.3 Static models . . . . .	14
1.3 The origin of star clusters . . . . .	15
1.3.1 From gas to stars . . . . .	15
1.3.2 Substructure and early dynamical evolution . . . . .	18
1.3.3 Star formation efficiency and infant mortality . . . . .	18
1.4 Simulating star clusters evolution . . . . .	20
1.4.1 Hydrodynamical simulations . . . . .	20
1.4.2 Artificial substructure . . . . .	21
1.5 Binary stars . . . . .	23
1.5.1 What is a binary star ? . . . . .	23
1.5.2 Why binaries ? . . . . .	23
1.5.3 Multiplicity fraction . . . . .	24
1.5.4 Observed population . . . . .	24
1.5.5 Simulate binary populations in clusters . . . . .	25
1.6 NBODY6 . . . . .	26
1.6.1 Hénon units . . . . .	26
1.6.2 Block time-step . . . . .	27
1.6.3 KS-regularization . . . . .	27
1.6.4 Hermite integration scheme . . . . .	28
1.6.5 Ahmad-Cohen neighbour scheme . . . . .	30
<b>2 The Hubble-Lemaître fragmented model</b>	<b>33</b>
2.1 How to build a Hubble-Lemaître model . . . . .	33
2.1.1 Initial state . . . . .	33
2.1.2 Fragmentation . . . . .	34
2.2 Perturbation theory . . . . .	37
2.3 Analysis of the fragmented system . . . . .	37
2.3.1 Clump finding algorithm . . . . .	37
<b>3 Dynamical evolution</b>	<b>41</b>
3.1 Bla . . . . .	41
3.1.1 Scaling to physical units . . . . .	41
3.1.2 Collapse and virialisation . . . . .	42

3.2	Global mass segregation . . . . .	43
<b>4</b>	<b>Binary population evolution</b>	<b>47</b>
4.1	Shock . . . . .	48

# Historical foreword: from Aristotle to GPU computing

Physics was not built in a day. In this foreword, I attempted a summary of the intellectual development that led us to our current state of knowledge. I did my best to honor the brilliant minds that made all of this possible. However, as everything in life, it should be taken with caution and a critical mind. I learned many things researching for this, I'm sure you will too if you follow the (minimal) citation trail I traced.

## Motion

For two thousand years, Aristotle physics dominated European philosophy. Rocks fell to the ground because they wanted to join their element, objects in the sky were attached to eternal rotating crystal spheres, and motion was either natural or violent, the latter needing a continuous force to exist. As the importance of projectiles grew in middle-age warfare, some improvements were made to explain trajectories, such as the impetus, a "contained source of motion" imprinted to a projectile by the thrower. Introduced by Philopon in the 6th century and relayed by Avicenne in the 11th century, it was properly formalized by Jean Buridan in the 14th century in his "Questions on Aristotle's Metaphysics". Buridan's impetus had a lot in common with momentum, in that it was proportionnal to mass and velocity, but could be circular, as shown by this description of celestial motion from Buridan ([Clagett, 1959](#)):

God, when He created the world, moved each of the celestial orbs as He pleased, and in moving them he impressed in them impetuses which moved them without his having to move them any more...And those impetuses which he impressed in the celestial bodies were not decreased or corrupted afterwards, because there was no inclination of the celestial bodies for other movements. Nor was there resistance which would be corruptive or repressive of that impetus.

Despite the conceptual mistake of a circular momentum, Buridan, with this text, is the first to include the motion of celestial bodies in the same framework used for everyday, terrestrial motion. The impetus is not a good model, but it is a model for everything in the universe. No more eternal crystal spheres, everything in the universe must obey the same laws. Scientific revolutions do not happen in a vacuum: Buridan and others paved the way for the intellectual landslide of the 16th and 17th century.

## Geocentrism and heliocentrism

While the concept of motion was slowly being refined, our vision of the universe was undergoing some faster changes. The dominant system in Europe since 150AD was the Ptolemaic geocentric model: the Sun and planets went around the Earth, following convoluted trajectories made of circles within circles called epicycles. Though complex, this system was consistent with Aristotle principles of celestial spheres and was accurate to a reasonable extent. Some alternate geocentric

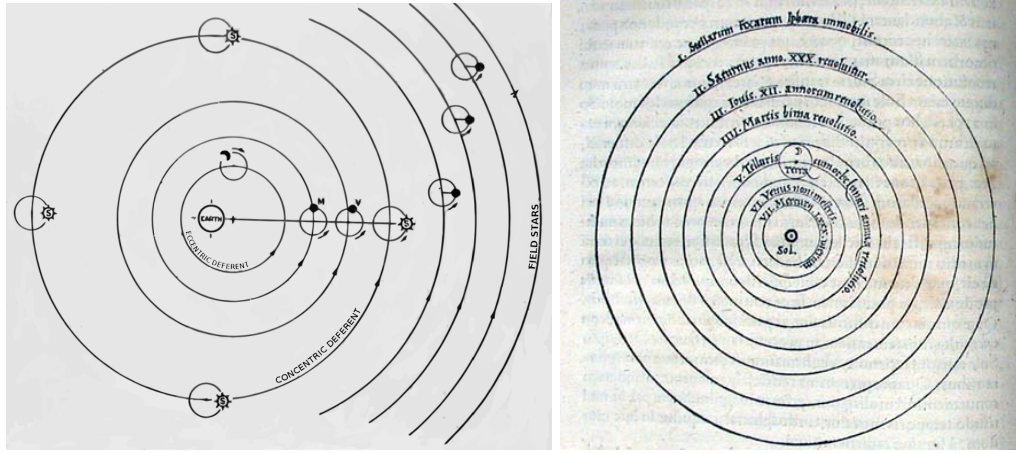


Figure 1: Left: Depiction of the Ptolemaic geocentric system, the equant is not shown . Right: Copernicus illustration of his own heliocentric system, from *De revolutionibus*.

models were proposed by arab astronomers, such as Nasir ad-Din at-Tusi and Ibn al-Shatir, as well as rejected attempts to heliocentric models.

Nicolaus Copernicus studied astronomy in Cracow and Bologna, under the influence of hard critics of the ptolemaic system. Strangely, this criticism was not fueled by observations, but by astrology. Astronomy and astrology were closely intertwined, and the chaotic structure of the ptolemaic system made astrological considerations complicated (Barker et al., 2014). In a quest for consistency and simplicity, Copernicus proposed his heliocentric system, published in *De revolutionibus orbium coelestium* in 1543, the year of his death, in which all planets went around the sun, in the correct order. However, clinging to circular orbits, Copernicus had to preserve ptolemaic workarounds such as epicycles.

The astronomical evidence was, at the time, paradoxically against him. The apparent size changes of planets could not be measured yet, as well as stars parallaxes, contradicting heliocentrism. The idea of a moving Earth implied some effect on falling bodies (known today as coriolis effect) which were also not measurable at the time. Building on this apparent counter-evidence and on the work of indian astronomer Nilakantha Somayaji, Tycho Brahe, the most renowned astronomer of his time, proposed an alternative model known as the Tychonic system in the late 16th century (Ramasubramanian, 1998). Brahe maintained the Earth as the center of the universe, circled by the sun, itself orbited by all other planets. The system was very efficient and was quickly adopted by the Church and considered in compliance with the Holy Scriptures.

However, the seed of heliocentrism was planted in european scientific minds. The idea exalted the impetuous and visionary Giordano Bruno, who pushed the decentralization of Earth to the extreme, claiming stars were other suns, harboring other planets, which themselves could sustain intelligent life. For this, his rejection of catholic dogma and his vehement refusal of retraction, Bruno was burned at the stake on the Campo de Fiori in 1600. Bruno, the fiery dialectist, despised geometry and believed the mind alone could unravel any mystery.

Johanes Kepler believed in geometry, in consistency and in observations. Ardent supporter of copernicism, he convinced Tycho Brahe to grant him access to his astronomical data, unsurpassed at the time. Focusing on the motion of Mars, Kepler, through trial and error, found out the planet was moving around the Sun following an ellipse. He formulated his first two laws of planetary motions. Further exploration led him to the third law. The three laws of Kepler were formulated, initiating the mathematisation of astronomy, and with it of all physics.

## The Starry Messenger

The father of modern astronomy, and precursor of modern science, Galileo Galilei was born in Pisa in 1564. For the first part of his scientific career, Galileo got famous for his lectures on mechanics and motion. Building on Buridan and Oresme's ideas, he expressed the mathematical form of free fall motion  $d = \frac{gt^2}{2}$ . Galileo also formulated what was essentially the future first law of motion from Newton.

In 1609, his passion for scientific instruments led Galileo to build his own "dutch perspective glass", or telescope, a pioneering optical device from the Netherlands. Once pointed at the sky, the device triggered an avalanche of observations who would forever bury the aristotelitian view of perfect and unchanged heavens. Moving Jupiter satellites, Moon craters and mountains, millions of stars in the Milky Way, these were consigned into *Sidereus Nuncius* (Starry messenger), the first scientific publication of astronomical observations (Galileo, 1610).

Strong advocate of copernicism, but lacking proper evidence, Galileo caused a large controversy with his *Dialogue Concerning the Two Chief World Systems* published in 1632, a pamphlet against the ptolemaic system, presenting (arguably unintentionally) one of its advocates as a simpleton. Despite his friendship with the pope, he had to retract his work and reject copernicism. Galileo spent the rest of his life on house arrest. Observational evidence at the time was still on the side of geocentrism, but the extent of the backlash against Galileo showed the febrility of a Church having absorbed Ptolemy and Aristotle principle into its doctrine, in a time where the debate was shifting from theology to physics and observations.

The relativity of motion is often attributed to Galileo, as he includes it in its controversial pamphlet, stating that a traveller inside a ship sailing smoothly would not be able to tell he's moving. Thus, people could be standing on a moving Earth without feeling it. However, this thought experiment was nothing new at the time and had been a recurring theme of mechanical philosophy since Buridan. Oresme, Copernicus and Bruno had been building on the idea, expanding and improving it, developing over the centuries an implicit understanding of inertia, until Bruno actually gives it a name: *virtù*. Galileo may have met Bruno himself, and had surely been influenced by his writings (De Angelis & Santo, 2015). Galileo's formulation was clearer, and part of a larger understanding of motion, introducing the concept of reference frame. After Copernicus decentralized the Earth, Galileo decentralized human subjectivity itself, setting the scene for the revolution to come.

## On the shoulders of giants

Isaac Newton is without a doubt the father of modern mathematical science. Admitted in Cambridge in 1661, Newton supplemented the -still- official aristotelitian teaching with more modern authors: Copernicus, Galileo, Kepler, and most of all, Descartes. The french philosopher had a profound impact on the young student, rooting his love for mathematics and deductive reasoning. However, while Descartes showed disdain for experimentation, Newton was an acute observer of the natural world.

In 1666, while in his mother's farm, having been forced out of Cambridge by the Plague, Newton began his reflexion on the motion of celestial bodies. He derived from Kepler's law that the Sun had to exert an inverse squared distance attraction on the planets. Extending the concept to the Earth, moon, and a famous apple, Newton found a way to verify his hypothesis, using data from Galileo mechanical studies on the strength of Earth attraction. The wrong estimate of Earth radius he used at the time introduced a discrepancy which put the young man off his *gravitas* studies for 18 years.

Edmond Halley, astronomer and friend of Newton, having heard of Newton inverse squared law, urged him in 1684 to communicate his work the Royal Society. With a new accurate measure of Earth radius and confronted to a concurrent claim to his law from Robert Hooke (Kramer, 1982), Newton capitulated to Halley's eager enthusiasm and communicated his work in the

famous *Philosophi Naturalis Principia Mathematica* (Newton, 1687). Published at Halley's own expense, the Principia shook all of Europe. Newton had invented Calculus (in parallel of Leibniz) and applied it to derive the universal law of Gravitation.

$$F = G \frac{m_1 \cdot m_2}{r^2} \quad (1)$$

Where:

- $F$  Gravitational attraction between object 1 and object 2
- $G$  Gravitational constant,  $6.67408 \cdot 10^{-11} m^3 kg^{-1} s^{-2}$  (Pavese, 2015)
- $m_i$  Masses of object 1 and 2
- $r$  Distance between object 1 and 2

Though Newton was part of continuous line of geniuses and innovative minds building from each others, as he puts it "If I have seen further it is by standing on the shoulders of giants" (Maury, 1992), his input was truly revolutionnary. He made large advances in optics and mathematics, and created a consistent mathematical framework to compute motions, essentially founding modern science and sowing the seeds of the industrial revolution. This framework is summed up by Newton's three laws of motion (from recent translation Cohen I. B. 1999):

Law I : Every body persists in its state of being at rest or of moving uniformly straight forward, except insofar as it is compelled to change its state by force impressed.

Law II: The alteration of motion is ever proportional to the motive force impress'd; and is made in the direction of the right line in which that force is impress'd.

Law III: To every action there is always opposed an equal reaction: or the mutual actions of two bodies upon each other are always equal, and directed to contrary parts.

The second law can be mathematically formulated in more modern terms:

$$\sum \mathbf{F} = \frac{d\mathbf{p}}{dt} \quad (2)$$

Meaning the sum of all forces  $\mathbf{F}$  applied to an object is equal to the time derivative of its momentum  $\mathbf{p} = m \cdot \mathbf{v}$ .

### The n=3 body problem

As the Enlightenment brought a scientific revolution in many fields, I will now limit the discussion to the development of celestial mechanics, while acknowledging input from other fields.

While the two-body problem had been solved by Newton and expanded by Bernoulli in 1710 (Barrow-Green, 1997), in the 18th century the three-body problem remained the object of much investigation and development. A general solution for the Earth-Moon-Sun system would have had applications on nautical astronomy and trans-continental navigation. Extended analytical work by d'Alembert, Clairaut, Euler and Lagrange led to the development of early families of approximate solutions or exact solutions to special cases.

From 1773 to 1793, Joseph-Louis Lagrange, helped by his invention of Lagrangian mechanics, would make a lot of advances on the three-body problem. He introduced the concept of potential and discovered libration points (later known as Lagrange points). In the same time, Pierre-Simon de Laplace proved the stability of the solar system using a newly developped perturbation theory. The solar system dynamics were being unraveled, with finely tuned perturbation computation, but the general three-body problem remained unsolved.



In 1888, Henri Poincaré, greatest mathematician of his time, submitted an entry to a contest organized by the King of Sweden Oskar II. The goal was to determine a usable solution to the  $n$ -body problem, for any given  $n$ . While Poincaré does not submit a complete solution, he wins the contest by presenting an in-depth exploration of the phase-space of the restricted three-body problem, which would later give rise to the Chaos theory, see [Yoccoz \(2010\)](#). Poincaré managed to prove that the three-body problem had no solution involving simple functions.

Contrary to popular belief, the three-body problem *has* a solution, it was derived by Karl F. Sundman in 1912 ([Sundman, 1912](#)). However, any attempt to obtain accurate trajectory predictions would face tremendous convergence time and is in practice unusable ([Belorizky, 1930](#)).

It is interesting to note that Elis Strömberg performed by-hand calculation of a three-body system, see [Aarseth \(2003\)](#); [Strömberg \(1909\)](#), prefiguring the advent of numerical orbit computation.

## The $n > 3$ body problem

”The Sun attracts Jupiter and the other planets, Jupiter attracts its satellites and similarly the satellites act on one another.”

By this sentence from the *Principia*, Newton formulates the  $n$ -body gravitational problem, an arbitrary number of massive bodies all interacting gravitationally, for the solar system. The ” $n > 3$ -body” problem didn’t receive a lot of attention at first, as the unruly three-body problem was on everyone’s mind, and a  $n > 3$ -body problem seemed abstract, the solar system example being appropriately dealt in approximations.

In 1764, Charles Messier resolved individual stars in Messier 4, a globular cluster, hundreds of thousands of stars grouped together. Many new clusters were to be found afterwards, extending the catalog of real-life  $n$ -body systems. However, nothing was known of their kinematics, the stars were, in a sense, suspended motionless in the sky. This was the case until the advent of Doppler spectroscopy, which allowed astronomer to measure stars velocities ([Doppler, 1842](#)). Stellar dynamics had begun.

The  $n > 3$ -body problem was still inaccessible, so scientists like James Jeans and Arthur Eddington decided to take the problem from the other hand, and took advantage of the large number of stars. Inspired by [Poincaré \(1906\)](#), both astronomers applied the statistical theory of gas to stellar systems, founding the field of stellar dynamics ([Jeans, 1916](#); [Eddington, 1916](#)).

An interesting experiment was conducted by [Holmberg \(1941\)](#) to understand the collision of two stellar systems (galaxies). With too few points to warrant a statistical approach, and before the rise of numerical integration, Holmberg modelled two galaxies with dozens of lightbulbs and photocells, measuring the attractive force with the amount of light received in each direction, taking advantage of the inverse squared fall of luminosity with distance, akin to gravity.

## The numerical age

The first numerical  $N$ -body computations were performed by Sebastian Von Hoerner in 1959 when visiting the University of Tübingen, on a Siemens 2002, a cutting edge calculator at the time. The very first had  $N=4$ . Then, Von Hoerner, back in Heidelberg, worked his way up to 16 stars, then 25, programming and debugging on punch cards. This story was told by Von Hoerner himself in [von Hoerner \(2001\)](#). He very quickly realized the importance of binary stars and their impact on computations. He was also able to confirm some theoretical prediction on cluster dynamics, and found an interesting radial density profile with a center cusp ([von Hoerner, 1960, 1963](#)).

There was two ways to increase the number of stars in simulations: buy a better computer or improve the algorithm. Sverre Aarseth got invested in the second path, which would take

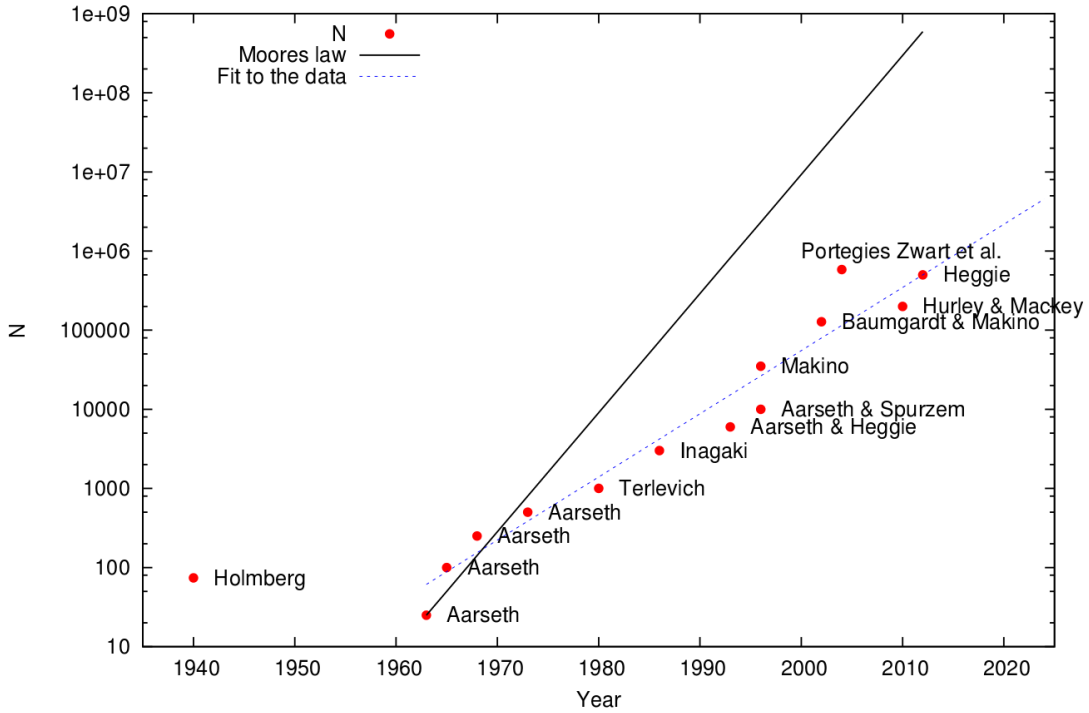


Figure 2: The evolution of the number of particles in N-body simulations. Solid line shows the Moore law. The figure was taken from [Bédorf & Portegies Zwart \(2012\)](#).

over his scientific life. Aarseth pioneered the use of individual time-step, changing the rate at which particles positions are updated, gravitational softening, allowing convergence for close approach, and polynomial prediction for force calculations ([Aarseth & Hoyle, 1964](#)). As power and optimization grew, investigations expanded, such as the interaction star-gas ([van Albada, 1968b](#)) and binary formation ([van Albada, 1968a](#)).

The 1970s brought two new important optimisation methods: KS regularization of close pairs ([Aarseth, 1972](#)) and Ahmad-Cohen neighbour scheme ([Ahmad & Cohen, 1973](#)). The number of stars in simulations kept growing, reaching 1000 with [Terlevich \(1980\)](#) and materializing into the *NBODY5* integrator. At this point various methods departing from a pure collisional calculation began to emerge, such as the simplified distant interaction with the [Barnes & Hut \(1986\)](#) tree algorithm.

To go beyond the regular improvement of computing power with time, a group of Japanese researchers, among whom Junichiro Makino, designed and built special purpose hardware for many-body problems: GRAPE ([Ebisuzaki et al., 1990](#); [Ito et al., 1991](#)). These cards vastly improved the speed of nbody simulations and were a milestone on the road to the parallelization of computing. With the force calculation directly implemented in the hardware, GRAPE dominated the field for 15 years.

The latest technological leap in Nbody simulations came from graphic cards, see [Bédorf & Portegies Zwart \(2012\)](#) for a more detailed historical perspective. Graphical Processing Units, or GPU, were originally designed for computer games visual rendering, applying the same transformations to a lot of pixels at the same time. These made them very efficient parallel computing machines for physics. Interest in GPU computing started to grow in the 2000s ([Nyland, Harris & Prins, 2004](#); [Elsen et al., 2006](#); [Portegies Zwart, Belleman & Geldof, 2007](#)) until the advent of usable GPU programming languages, like CUDA, in the late 2000s. At this point GPU were more efficient than GRAPE hardware for force calculation. Keigo Nitadori and Sverre Aarseth developed a GPU-accelerated version of the latest NBODY code, NBODY6, in 2012 ([Nitadori & Aarseth, 2012](#)).

Last year, 329 years after the publication of the *Principia*, a collisional nbody simulation of one million stars was performed with a modified version of NBODY6 running on GPU ([Wang et al., 2015](#)). Computers have made it possible for humans to study systems of incredible scales in space and time, only using the universal law of gravitation. N-body numerical integrators are the culmination of centuries of scientific development on the motion of massive bodies.



# CHAPTER 1

## Introduction

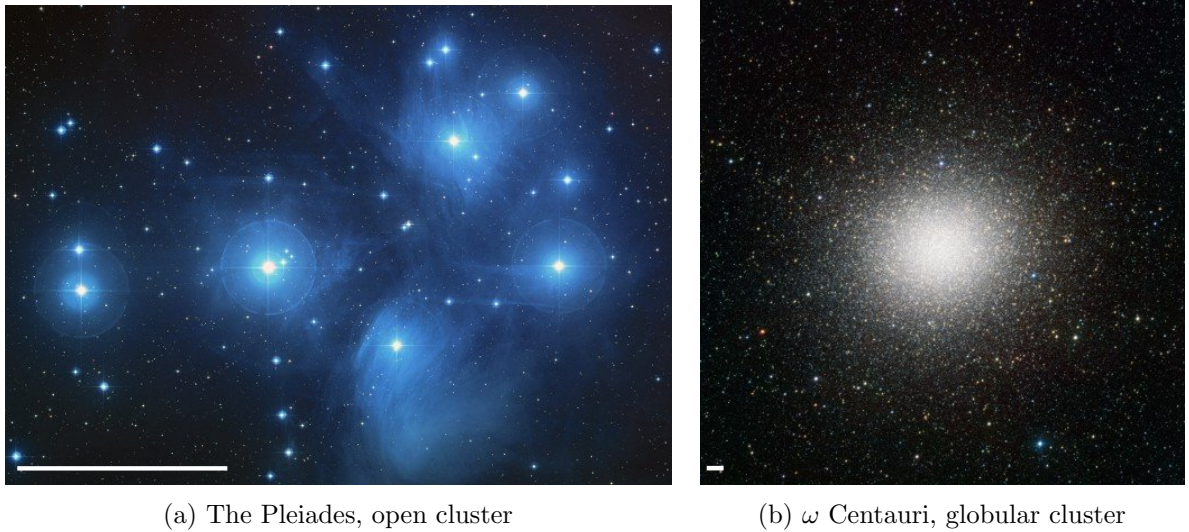


Figure 1.1: Examples of various types of cluster. White bars at the lower left of each pictures show 1 parsec. The dust present in (a) scatters starlight producing this blue haze. (b) contains one million stars and is the largest known star cluster in the Milky Way.

*Credits: NASA, ESA, AURA/Caltech; ESO/INAF-VST/OmegaCAM*

## 1.1 Introduction to star clusters

What is a star cluster ? The widest definition possible for a star cluster is "An area of the sky with visibly grouped stars". However, this includes galaxies and random line-of-sight groups. We are interested in physical objects, smaller than galaxies, in which stars are, if not bound, at least under direct mutual gravitational influence. Such objects include open clusters, globular clusters or associations. [Lada & Lada \(2003\)](#) adopted the following definition: a cluster is a stellar system with  $N > 35$  and a density  $\rho > 1 \text{ M}_{\odot}/\text{pc}^3$ . These objects can either dissolve in less than a million year or remain bound for billions of years. In the last century, thanks to the improvement of observation techniques, many clusters have been discovered and their origins are progressively unravelled.

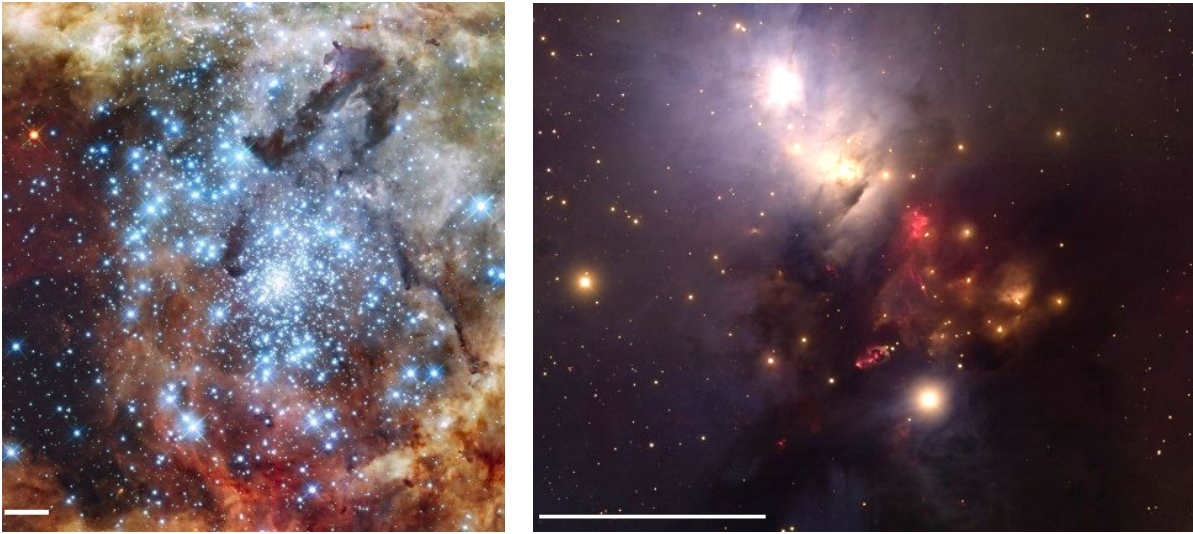
### 1.1.1 Why study them ?

Clusters are the result of bursts of star formation in Giant Molecular Clouds. All stars within a cluster were born approximately at the same time, which explains the sustained interest of the scientific community for star clusters: they are the best available stellar physics laboratories, a large population of stars sharing the same age and distance to Earth. The age of the cluster can be derived from the most massive surviving stars in the population, as stars have lifetimes inversely correlated with their mass. Overall, integrated spectral features from all members of a star cluster can provide a wealth of information.

As we will see, clusters are also crucial to understand stellar formation. They harbour the most massive and young stars, which cause large-scale ionisation, winds and shockwaves from their explosive death in supernovae. Massive stars caused the re-ionization of the entire known universe 400 Myr after the Big Bang. To understand massive stars is to understand star formation, and to understand star formation is to understand star clusters.

### 1.1.2 Types of star clusters

Star clusters are historically divided into two main categories: globular clusters and open clusters. As observational techniques improved, categories tended to blend into a spectrum of size,



(a) R136, Young Massive Cluster

(b) NGC 1333, embedded cluster

Figure 1.2: Examples of various types of cluster. White bars still show 1pc. (a) is surrounded by its primordial nebula while (b) is still inside it, the picture is a composite of visible and infra-red light. *Credits: NASA, ESA, F. Paresce; T. Rector (U. Alaska Anchorage), H. Schweiker*

age, and dynamical state, with Young Massive Clusters, embedded clusters and OB associations. Several of these categories have significant overlap, but each one emphasizes a particular characteristic of star cluster, thus these are useful for a comprehensive discussion.

**Globular clusters** are old and massive stellar systems. Most of them are older than 10 Gyr and more massive than  $10^4 M_{\odot}$ . The most massive known Globular cluster in the Milky Way is  $\omega$  Centauri, with  $4 \cdot 10^6 M_{\odot}$  (D’Souza & Rix, 2013), see ref 1.1b. They only contain stars, without any dust or gas. The 150 known globular clusters in the Milky way are scattered in the disk and the halo, with a higher concentration near the bulge (Harris, 1996).

**Open Clusters** are lighter objects, rarely more massive than  $10^3 M_{\odot}$ . They are also younger, with ages ranging from a few Myr to a few Gyr (Dias et al., 2002). In fact, open clusters do not have a clear definition other than the implicit and historical characteristic of ”not being a globular cluster” and have a very wide range of characteristics. Overall, they are faint, sometimes irregular and volatile objects. Their small mass and lower density make them vulnerable to tidal disruption from passing massive clouds on nearby orbits. The pleiades are a famous example, see ref 1.1a

**OB associations** contain even less stars than open clusters, a few dozens in average. They get their name from the very massive luminous O and B type stars they contain, sometimes more massive than  $50 M_{\odot}$ . Such stars do not survive more than a few million years, OB association are thus young objects located in active star forming regions. They are often found near other associations, in a hierarchical structure. Their density is much lower than a typical cluster, about  $0.1 M_{\odot} \text{pc}^{-3}$  (Wright et al., 2014), in fact most are unbound and dissolving objects. See Garcia et al. (2010) for a detailed census and description of the OB associations in IC 1613.

**Embedded clusters** are the youngest star clusters in the sky. Most of the stars, protostars and cores are still inside their primordial cloud, dust obscuring their optical light. The development of infrared astronomy unveiled the internal structure of these objects. As the gas is fully evacuated by 10Myr (Lada & Lada, 2003), embedded clusters are younger and



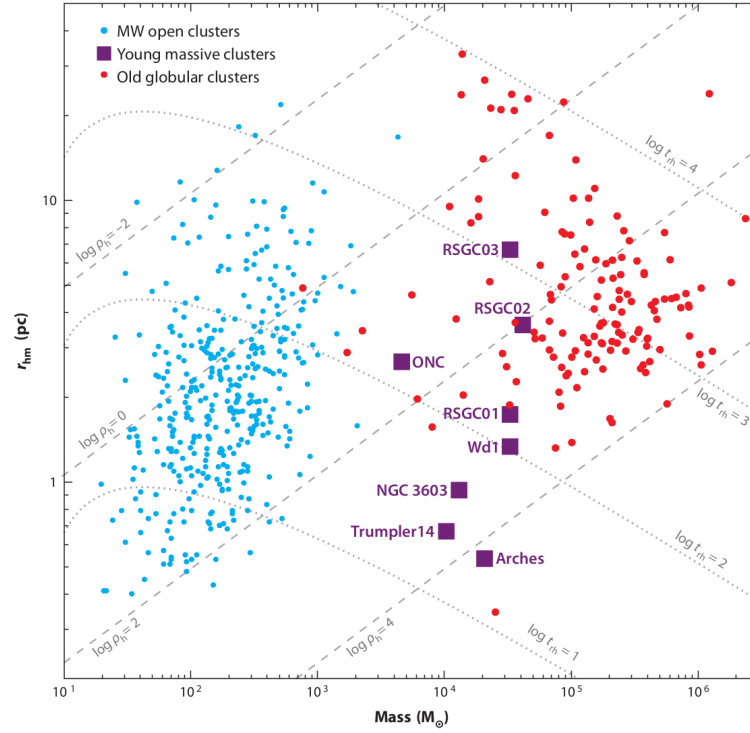


Figure 1.3: Radius-Mass Diagram for Milky Way clusters. Blue dots are open clusters, red dots Globular clusters and purple squares show Young Massive Clusters. Dashed lines show constant density within half-mass radius  $\rho_h = 3M/8\pi r_{hm}^3$  and dotted lines show constant relaxation time. The plot was taken from the review [Portegies Zwart, McMillan & Gieles \(2010\)](#).

observed to be substructured (?). Some have ongoing star formation, like NGC 1333, a very young embedded cluster with both proto-stars and stars, see [Foster et al. \(2015\)](#) and Fig 1.2b.

**Young Massive Clusters**, or YMCs, are considered to be globular cluster progenitors. The review by [Portegies Zwart, McMillan & Gieles \(2010\)](#) provides a definition of YMCs: bound systems more massive than  $10^4 M_\odot$  and younger than 100 Myr. Only a handful of such systems are known in the milky way (see Fig 1.3). The most studied YMC of the galactic neighborhood is R136, with a mass  $\sim 10^5 M_\odot$  ([Andersen et al., 2009](#)), see Fig 1.2b. It is located in the Tarentula nebula, the most active known star forming region in the local group, inside in the Large Magellanic Cloud <sup>1</sup>. YMCs are found in large number in intense star forming environment such as starburst galaxies and galaxy mergers like the Antenna galaxies ([Whitmore et al., 2010](#)).

”All stars form in clusters” is a recurring statement in the field of stellar and cluster formation. Near Infra-Red (NIR) studies of star forming region yielded an star formation rate from embedded clusters of  $\sim 3 \cdot 10^3 M_\odot \text{ Myr}^{-1} \text{ kpc}^2$  ([Lada & Lada, 2003](#)) while the same estimation for field stars in the milky way gives  $\sim 3 - 7 \cdot 10^3 M_\odot \text{ Myr}^{-1} \text{ kpc}^2$  ([Miller & Scalo, 1979](#)). Another clue at the clustered nature of star formation is that high-mass O stars are for the vast majority, clustered, see [de Wit et al. \(2005\)](#). Due to their short life, O stars are often observed at the very location of their birth, or not very far. However, some work by, e.g, [Gutermuth et al. \(2011\)](#) seemed to point at a spatially hierarchical star formation. So stars do form in clusters, as in, in groups, but these groups are diverse and their dynamical evolution is complex.

<sup>1</sup>A dwarf irregular galaxy orbiting the milky way.



## 1.2 Some important dynamical concepts

### 1.2.1 Virial theorem

A self-gravitating system is a system bound by its own gravity. This applies to a star, a molecular cloud, a star cluster or a galaxy. In all cases, gravity is set against a counteracting force that prevents the total collapse of matter into a single point. This force can be pressure for stars and clouds, but for stellar systems such as clusters and galaxies, it is the agitation of its components, the kinetic energy of the stars. Other forces include magnetic pressure or tidal fields.

The exchange between the gravitational potential energy and the kinetic energy follows the famous virial theorem, written in the general form (McKee & Ostriker, 2007; Binney & Tremaine, 2008):

$$\frac{1}{2} \frac{d^2 I}{dt^2} = 2(E_k - E_{k,s}) + E_p + E_{tides} + E_m \quad (1.1)$$

with  $I$  the moment of inertia,  $E_k$  the kinetic energy,  $E_p$  the potential energy.  $E_{k,s}$  a thermal pressure surface term,  $E_{tides}$  the energy injected by a tidal field and  $E_m$  the magnetic pressure. For a stationnary system,  $\frac{1}{2} \frac{d^2 I}{dt^2} = 0$ , and in a purely gravitational system with  $N$  particles, there is no thermal or magnetic pressure. Finally, if we consider an isolated system,  $E_{tides} = 0$  and the virial theorem can be written in its more common form:

$$2E_k + E_p = 0 \quad (1.2)$$

with :

$$E_k = \sum_{i=1}^N m_i v_i^2 \quad \text{and} \quad E_p = - \sum_{i=1}^N \sum_{j>i}^N \frac{G m_i m_j}{\|\mathbf{r}_i - \mathbf{r}_j\|}. \quad (1.3)$$

We define the virial parameter  $Q$  as:

$$Q = - \frac{E_p}{E_k}, \quad (1.4)$$

$Q = 0.5$  is a system in virial equilibrium. If the amplitude of the velocities is not sufficient to counteract the current value of potential energy,  $Q < 0.5$ , the system is said to be dynamically cold, or *subvirial*. While if the stars are too close together compared to the velocity amplitudes,  $Q > 0.5$ , the system is hot and *survirial*. If  $Q > 1$ , the total energy is positive and the system is unbound.

### 1.2.2 Dynamical timescales

Dynamical systems tend to virial equilibrium. In such self-gravitating systems, it is useful to define a few dynamical time scales. The most simple one is the **crossing time**, defined as:

$$t_{cr} = \frac{R}{\sigma} \quad (1.5)$$

with  $R$  the typical radius of the system and  $\sigma$  the velocity dispersion. It is the typical time it takes for a particle to cross the system. Another crucial timescale in stellar dynamics is the **relaxation time**. Binney & Tremaine (2008) define it as:

$$t_r \simeq \frac{0.1N}{\ln N} t_{cr}. \quad (1.6)$$

In a self-gravitating system, stars have orbits. If  $N$  is large enough, the potential inside the system is smooth and stars have stationnary orbits. The relaxation time is the timescale at

which the impact of numerous encounters a star endures is comparable to the motion of its initial orbit. In other words, the initial conditions of a system are dynamically erased by collisional evolution after a relaxation time.

In a relaxed cluster, the core is dense with a high velocity dispersion, whereas the outskirts, the halo, is less dense and stars are slower. The definition from equation (1.5) and (1.6) imply the relaxation time changes with distance to the center. It is therefore useful to define a global timescale for the whole system, the **half-mass relaxation time** defined by [Heggie & Hut \(2003\)](#):

$$t_{rh} \simeq \frac{0.138}{\ln N} \sqrt{\frac{N}{Gm}} R_h^{\frac{3}{2}} \quad (1.7)$$

with  $m$  the mass of a star and  $R_h$  the half-mass radius. Let us compute two examples, taking  $G$  in appropriate units:

$$G \simeq 4.48 \times 10^{-3} \text{ pc}^3 \text{ Myr}^{-2} \text{ M}_{\odot}^{-1}. \quad (1.8)$$

A cluster with 1000 stars of  $0.5\text{M}_{\odot}$  and  $R_h = 1 \text{ pc}$  has  $t_{rh} = 13 \text{ Myr}$ , while a cluster with  $10^6$  stars of the same mass and a  $R_h = 6 \text{ pc}$  have  $t_{rh} = 3.1 \text{ Gyr}$ .

Equations (1.6) and (1.7) assume identical stellar masses in the system. In a real cluster, stars have different masses, differently affected by collisional evolution. The most massive stars cause gravitational focusing and exchange energy with other stars at a higher rate. They lose their energy to lighter stars, progressively sinking at the center. [Heggie & Hut \(2003\)](#) give an estimation of the segregation timescale  $t_{seg}(m_1)$  of a mass  $m_1$ :

$$t_{seg}(m_1) = \frac{m_1}{\langle m \rangle} t_{rh} \quad (1.9)$$

so a  $30 \text{ M}_{\odot}$  star in the previous 1000 star cluster will have a relaxation time of  $\frac{0.5}{30} 13 = 0.21 \text{ Myr} = 210,000 \text{ years}$ , much faster. A mass spread in a system speeds up considerably its collisional evolution.

### 1.2.3 Static models

It is useful to have a static reference model for a self-gravitating system at equilibrium. Considering a relaxed system with enough particles, one can use a statistical description to model its evolution, namely the "collisionless Boltzmann equation":

$$\frac{\partial f}{\partial t} + \mathbf{v} \cdot \nabla_r f - \nabla \Phi \cdot \nabla_v f = 0 \quad (1.10)$$

with  $f(\mathbf{r}, \mathbf{v}, t)$  the phase space distribution and  $\Phi$  the gravitational potential. There are several solutions to this equations, these are "static" models for star clusters as they are considered in equilibrium. Of course, the collisional equation can never be fully neglected and these models are approximations. We present here two models: Plummer and King. Both have a constant density in the center, the core, but they differ by their general behaviours.

The **Plummer model** is a simple model with a null potential at infinity. It is defined by its potential as a function of radius ([Binney & Tremaine, 2008](#)):

$$\Phi(r) = -\frac{GM}{\sqrt{r^2 + b^2}} \quad (1.11)$$

with  $b$  the Plummer parameter, setting the depth of the central potential and the core radius. From this expression, one can derive the radial density distribution:

$$\rho(r) = \frac{3M}{4\pi b^3} \left(1 + \frac{r^2}{b^2}\right)^{-\frac{5}{2}} \quad (1.12)$$

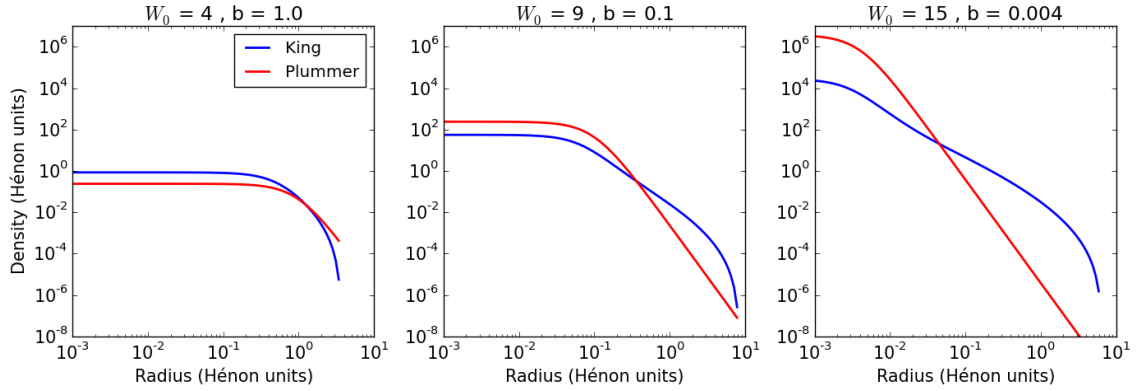


Figure 1.4: Comparison of King and Plummer models density as a function of radius, for similar core radii.

Equation (1.12) makes the computational generation of a cluster straightforward, which is why the Plummer model has been widely used in numerical simulations of star clusters. However, a Plummer model theoretically extends to infinity, and is not consistent with many globular cluster observations. Another, more complex, model has the observers on his side. The **King model** has been successfully used to fit light-profiles of globular clusters (King, 1981). It is defined as a distribution in energy:

$$f_k(E) = \begin{cases} f_0 \left( e^{-2j^2 E} - e^{-2j^2 E_0} \right), & \text{if } E < E_0. \\ 0, & \text{otherwise.} \end{cases} \quad (1.13)$$

with  $j$  a free parameter. The core radius can be tuned through a parameter  $W_0 = 2j^2(E_0 - E_c)$  with  $E_c$  the rest energy at the center.

The main difference with the Plummer model can be seen in Fig 1.4: for a given core radius, King's density decreases slower than Plummer, but does fall to zero at a given radius contrary to Plummer that continues to infinity.

## 1.3 The origin of star clusters

### 1.3.1 From gas to stars

The interstellar medium, or ISM, is made of dust and gas in various phases, densities and temperatures, ranging from a hot ionized medium ( $T > 10^5 K$  and  $n < 0.01 cm^{-3}$ ) to a cold neutral medium ( $T < 100 K$  and  $n > 10 cm^{-3}$ ), see Field, Goldsmith & Habing (1969). Finally, in colder denser regions,  $T \sim 10 K$  and  $n > 30 cm^{-3}$ , the hydrogen takes molecular form  $H_2$  in what is called molecular clouds. The dust contained in these regions makes them optically thick, obscuring background stars. These "holes in the sky", as William Herschel exclaimed upon the Dark Ophiucus Nebula (Houghton, 1942), come in different sizes, from the "bock globules" to Giant Molecular Clouds (GMCs). The interstellar dust absorbs the light in the visible and re-emits it in the infrared, thus the advent of infrared astronomy unveiled the interior of molecular clouds. In particular, recent observations with the Herschel Space Observatory showed a prevalence of filaments in clouds, see André et al. (2010).

Star formation occurs in the higher density clumps or filaments inside the clouds. The origin of these overdensities has been the object of extensive theoretical development for 60 years. Turbulent motion was very early on designated as the main cause of overdensity. Turbulence is the transfer of energy from large scales to small scales, creating motions on small scales from a large energy driver. The well known Kolmogorov incompressible turbulence is hardly applicable

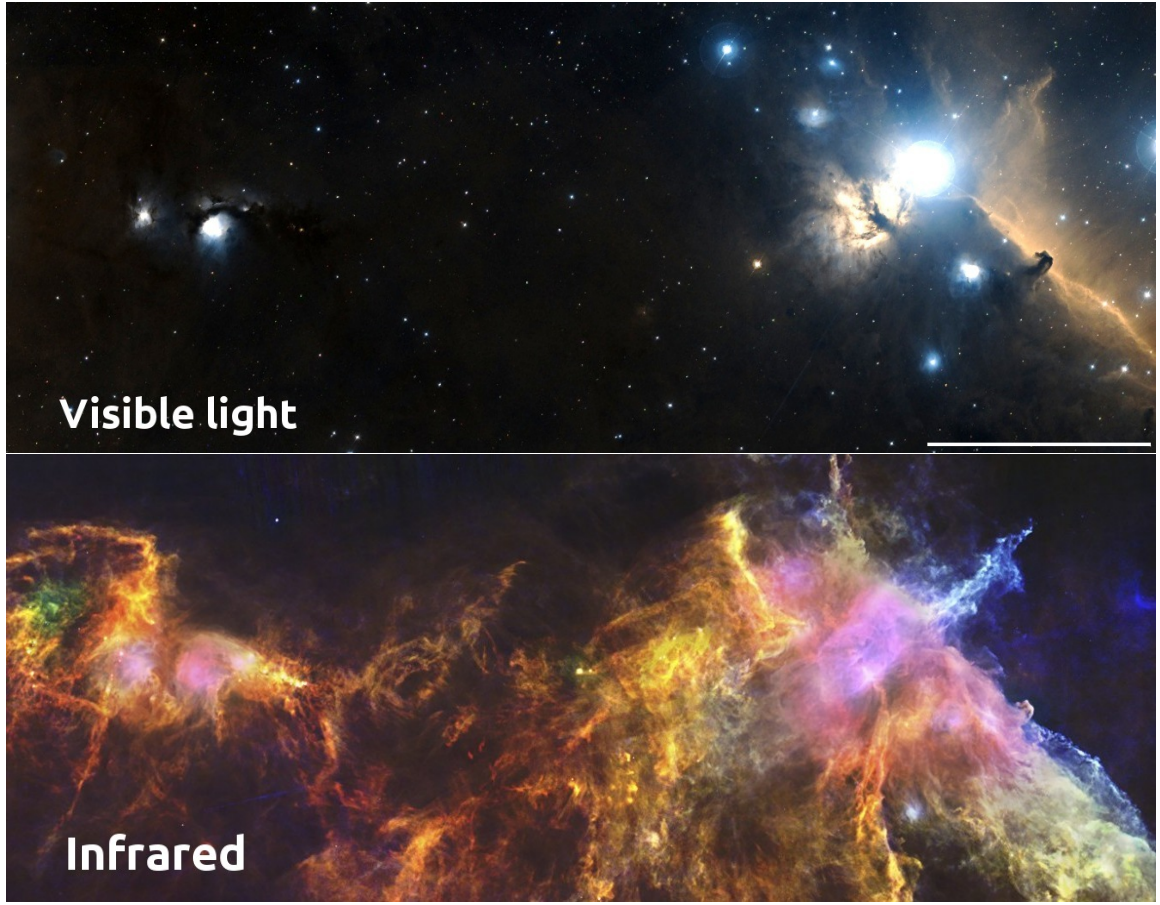


Figure 1.5: Visible light and infrared view of a part of the Orion star forming complex. Horsehead nebula is visible on the right, as well as the very bright star Alnitak, part of the Orion belt. NGC 2071 and 2068 are visible on the left. Pink infrared coloring shows radiation from very bright young massive stars forming in the cloud. Colder filaments are visible all around. White on lower right of visible shows 1 parsec. *Credits: Digitized Sky Survey; ESA/Herschel/PACS.*

to the ISM, as it is highly compressible (Scalo et al., 1998), instead, molecular clouds are subject to supersonic turbulence, or Burgers turbulence (Frisch, Bec & Villone, 2001). Nearby supernovas or tidal perturbation feed energy into the cloud, which is transferred through turbulence to smaller scales as supersonic internal motions, shocks forming overdense sheets. McKee & Ostriker (2007) argue that filaments originate both from the intersection of such sheets and the primordial morphology of the cloud, as self-gravitating pressureless matter condense as filaments (Springel et al., 2005).

Individual condensates of matter called cores form in clumps and filaments, these are stellar seeds (Fig 1.6a). To collapse, they have to overcome their magnetic and thermal pressure and their internal turbulence. The idealized picture of an hydrodynamical collapse relies on an estimation of the Jeans length  $\lambda_J$ , the maximum wavelength of a density perturbation in a uniform gas above which pressure cannot respond fast enough and gravitational collapse is triggered. The corresponding Jeans mass  $M_J$ , of diameter  $\lambda_J$  is the minimum mass of a cloud to collapse. These quantities are derived in Binney & Tremaine (2008) and are expressed

$$\lambda_J = \sqrt{\frac{\pi}{G\rho}} c_s \quad (1.14)$$

$$\simeq 0.2 \text{ pc} \left( \frac{c_s}{0.2 \text{ km.s}^{-1}} \right) \left( \frac{n}{10^3 \text{ cm}^3} \right)^{-\frac{1}{2}} \quad (1.15)$$



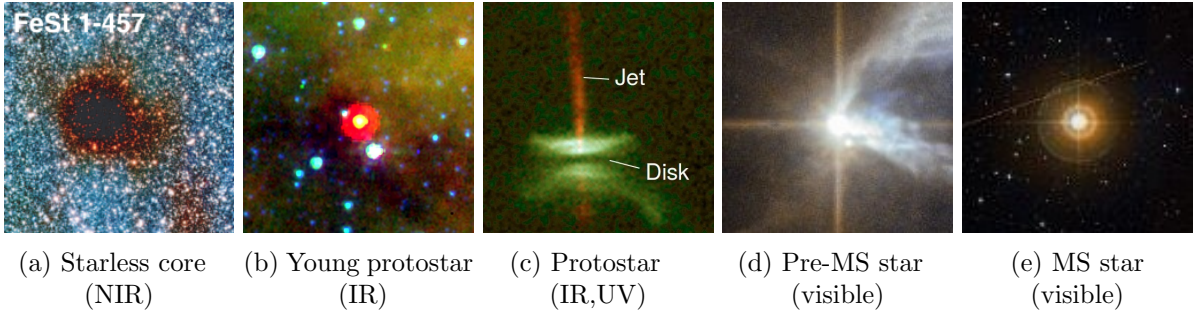


Figure 1.6: Stages of stellar birth. (a) is just cold molecular gas and contains no central source yet. (b) is more advanced, though hidden in visible light, its central protostar shines in infrared. The protostar in (c) is actively accreting its disk and produces jets. (d) is a pre main-sequence star, free from its envelope and surrounded by primordial gas. (e) is the mature stellar stage: the main sequence. *Credits: Kandori et al. (2005); NASA/JPL-Caltech/Evans, N; Burrows, C/HST-NASA; ESA/Hubble & NASA; DSS*

$$M_J = \frac{4\pi}{3} \rho (\lambda_J)^3 = \left(\frac{\pi}{6}\right) \frac{c_s^3}{G^{\frac{3}{2}} \rho^{\frac{1}{2}}} \quad (1.16)$$

$$\simeq 2.7 M_\odot \left(\frac{c_s}{0.2 \text{ km.s}^{-1}}\right)^3 \left(\frac{n}{10^3 \text{ cm}^{-3}}\right)^{-\frac{1}{2}} \quad (1.17)$$

with  $c_s$ ,  $\rho$  and  $n$  the local sound speed, density and number density. These are the typical values expected for a prestellar core with such sound speeds and number densities. The molecular gas remains isothermal throughout the collapse, as the center radiates away the thermal energy from the increased density. When density reaches  $10^{10} \text{ cm}^{-3}$ , the dust mixed in the protostellar material turns the core of the cloud optically thick, energy cannot be radiated away anymore, temperature rises and collapse stops. It continues to accrete material, increasing its central density and temperature. When  $T$  reaches 2000K, molecular hydrogen starts to dissociate, absorbing energy. This allows a second collapse, stopped when all initial molecular hydrogen has been dissociated. The resulting core is called a protostar (Fig 1.6b), its density profile is peaked in the center and reaches about  $10^{21} \text{ cm}^{-3}$  and a temperature of 20,000K. The protostar has a mass of  $\sim$  a thousandth of its future stellar mass, as most of it is acquired during the next phase, accretion. Angular momentum from the original cloud shapes the gaseous envelope into a disk around the protostar, and magnetic activity starts creating jets (Fig 1.6c). This stage has been divided into several classes, based on the Spectral Energy Distributions (SED) emitted by the objects, has the emission shifts from far infrared to mid, then near-infrared as the envelope is accreted. See Evans et al. (2009) for an historical description of the SED classes and Larson (1969) for a theoretical overview of the principles of collapse and protostellar formation.

After about a Myr, accretion stops and the object becomes a Pre-Main Sequence (PMS) star (Fig 1.6d). It slowly contracts, following the Hayashi track, first described by Hayashi (1961). The source of energy of the star is still gravitational contracting, until central temperature reaches  $10^6 \text{ K}$  and hydrogen starts fusing into Helium. The object enters the Main Sequence and begin its life as a proper star (Fig 1.6e).

### 1.3.2 Substructure and early dynamical evolution

Observations show molecular clouds are substructured (see e.g. Cambr sy 1999). This substructure can be seen as a fractal distribution (Elmegreen & Falgarone, 1996) or a network of filaments (Andr  et al., 2010), both consistent with compressible turbulence (McKee & Ostriker, 2007). This hierarchical structure is inherited by the cores and protostars that emerges

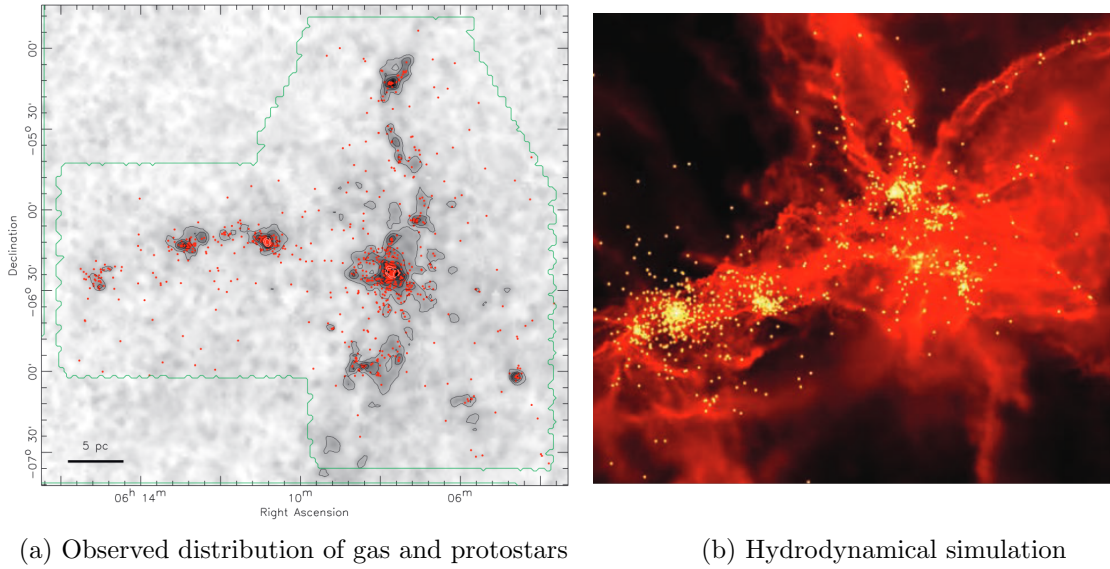


Figure 1.7: (a): observational data from the Monoceros R2 star forming region. Protostars are shown as red points and gas density (traced through extinction) is shown in greyscale. The figure was extracted from [Gutermuth et al. \(2011\)](#). (b): hydrodynamical simulation of a star forming region yellow points are star-like sink particles and red levels show gas density. The figure was extracted from [Bonnell et al. \(2011\)](#).

from the overdensities, as many observational studies of star forming regions shows ([Schneider & Elmegreen, 1979](#); [Hartmann, 2002](#); [Bressert et al., 2010](#)). Examples of substructured young clusters include the Taurus Ariga region,  $\rho$ -Ophiucus and Aquila, details and other examples can be found in both volumes of *The handbook of star forming region* [Reipurth \(2008\)](#).

However, other young clusters do not display such fractal, clumpy or filamentary structure. Instead, they are smooth, centrally condensed systems. The most known example is the Orion Nebula Cluster, or ONC. Located in the heart of the Orion complex, the largest and most active star forming region in the solar neighborhood, the age of the ONC is estimated to a few Myr. [Hillenbrand & Hartmann \(1998\)](#) found no clumps or filaments in the stellar distribution of the cluster, but a smooth distribution with a high density core formed by the Trapezium, a dense system of massive stars. This mass segregation, if not fully primordial, implies that some amount of dynamical evolution took place in the ONC since the formation of the stars. This dynamical evolution could have erased the initial substructures.

These observations point at a rough picture of substructured stellar formation and early evolution: when the newly born stars emerges in clumps, if the background tidal field is weak and the star forming region sits well inside its Roche radius, the clumps then progressively merge and converge to the system barycentre to form a unique, relaxed self-bound association over a course of a few crossing time. This picture is backed up to some extent by hydrodynamical simulations of fragmentation modes in the turbulent ISM ([Klessen & Burkert, 2000](#); [Bate, Bonnell & Bromm, 2003](#); [Mac Low & Klessen, 2004](#); [Offner, Hansen & Krumholz, 2009](#); [Maschberger et al., 2010](#)) and by recent observationnal clues that subclusters show dynamical traces of mergers ([Kuhn et al., 2015](#)).

Figure 1.8 shows the similarity of stellar distribution obtained by observations and simulations of star forming regions.

### 1.3.3 Star formation efficiency and infant mortality

In their seminal paper on embedded clusters, [Lada & Lada \(2003\)](#) coined the term "infant mortality" for young star clusters. Comparing the populations of embedded clusters and older

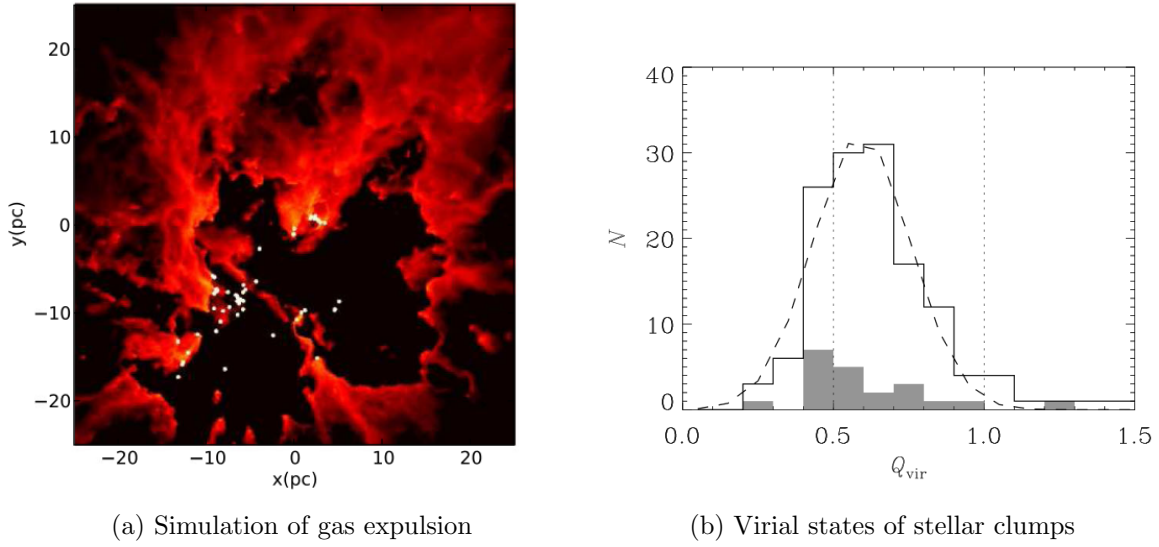


Figure 1.8: (a): hydrodynamical simulation of wind-induced gas expulsion around a small cluster, the figure was extracted from [Dale et al. \(2013\)](#). (b) virial parameter of stellar clumps in a star forming hydrodynamical simulation, ignoring the potential of the gas to predict their post-expulsion fate. The figure was extracted from [Kruijssen et al. \(2012\)](#).

open clusters, the authors concluded clusters had a 90% mortality rate before 10 Myr. This is explained by the traditional picture of gas expulsion in clusters: a portion of the gas in a molecular clouds form a group of protostars, which quickly accrete their envelope, then start nuclear burning. This portion is expressed as the star formation efficiency:

$$\epsilon = \frac{M_{\star}}{M_{\star} + M_{\text{gas}}} \quad (1.18)$$

with  $M_{\text{gas}}$  the remaining gas after star formation. This gas is thought to be ejected from the young cluster through photo-ionization (the UV radiation from massive stars ionize the neutral gas which heats up and expands), jets and outflows (young stars ejecting matter during accretion), winds (ejection of matter from stars surfaces at high speeds), and supernovae (shockwave from the explosive death of a massive star). The gas expulsion occurs on a dynamical time, see [Goodwin \(1997\)](#). Considering a young cluster in dynamical equilibrium, the loss of the mass of the gas on such a short timescale can unbound the system, as the stars velocities are now too high for the new potential well. The young cluster then dissolves following the gas expulsion. This picture is backed up by observations of young dissolving clusters ([Bastian & Goodwin, 2006](#)) consistent with corresponding numerical models ([Goodwin & Bastian, 2006](#)). Extensive analytical and numerical work have explored this process, e.g. [Tutukov \(1978\)](#); [Boily & Kroupa \(2003a,b\)](#), with an estimated minimum star formation efficiency of 30% to remain bound after gas expulsion.

However, the picture is more complicated than it seems. First, the efficiency of stellar feedback is a complex problem, winds, photionisation and supernovae have various impacts depending on the size and morphology of the clouds; they also seem to influence each other, for an overview of the problem see the serie of papers from [Dale & Bonnell \(2011\)](#); [Dale et al. \(2013\)](#) and references therein. Furthermore, recent hydrodynamical simulations such as [Pelupessy & Portegies Zwart \(2012\)](#) show the exact timescale of gas removal has a crucial importance on the fate of the cluster, with a slow removal allowing survival with  $\epsilon$  as low as 5%.

Finally, most of the previously mentioned simulations assumed a relaxed embedded stellar system. However, as mentioned in previous section, star formation is substructured. Dynamical evolution between clumps and subclusters occurs on timescales comparable to gas expulsion,

making the stellar spatial distribution of huge importance for survival, as shown by [Farias et al. \(2015\)](#). Hydrodynamical simulations (e.g [Kruijssen et al. 2012](#)) even point at subclusters being primordially quasi gas-less due to localized high  $\epsilon$ , thus increasing the importance of substructure over gas expulsion.

## 1.4 Simulating star clusters evolution

### 1.4.1 Hydrodynamical simulations

I invoked hydrodynamical simulations multiple times in the previous section. Let us look at them in more details. To model the formation of a star cluster from a core-less molecular cloud is no easy task. The model has to reproduce turbulence, core condensation, gravitational collapse, accretion, and for the most realistic ones, radiative cooling and stellar feedback. Two numerical path has been explored in the past: AMR and SPH.

Adaptative Mesh Refinement, AMR, is an Eulerian approach. The hydrodynamical equations (conservation of mass, momentum, the equation of state) are discretized and solved on a grid of cells following the finite volumes methods (see the RAMSES code, [Teyssier 2002](#)). Smoothed Particle Hydrodynamics, SPH, is a Lagrangian approach: instead of looking at inputs and outputs of matter in a cell, the gas is subdivided in particles free to move in the system. They are attributed a density, temperature and pressure. This method is akin the N-body integrator, and many SPH codes can work as purely gravitational integrators. SPH is popular in star formation simulations, as the problem is itself Lagrangian: grains of highly dense matter condensates and move around. Even if these codes can handle high density contrast, the collapse and formation of a protostar can still bring the numerical computation to a standstill. The usual workaround is the use of sink-particles: passed a given density threshold, several particles are merged into a single point-like object able to accrete any infalling matter. This works well though it suppresses any physical process below this accretion limit, usually a few to a hundred AU. ([Bate & Burkert, 1997](#)).

The precision, size and complexity of large scale cluster formation simulations have been steadily improving for 20 years (see [Turner et al. 1995](#); [Klessen & Burkert 2000](#); [Bate, Bonnell & Bromm 2003](#); [Offner, Hansen & Krumholz 2009](#); [Myers et al. 2014](#) and citations). Nevertheless, no simulation to date include realistic cooling processes, radiative and wind feedback, magnetic fields and dust chemistry, all at the same time. All these are crucial to achieve precise and realistic simulation of the star formation process. Moreover, one of the most detailed star formation simulations to date, e.g [Bate \(2012\)](#), only form a few hundred stars and evolved them for less than 0.2 Myr with a simulation run time of several months.

However, good results are already being achieved, see the short review by [Clarke \(2012\)](#). Stellar properties and general structure agree with observations and interesting results are being obtained. [Maschberger & Clarke \(2011\)](#) and [Moeckel & Clarke \(2011\)](#) have noted that massive stars tend to sit at the heart of gas clumps in hydrodynamical simulations, some as the result of merger events with low-mass proto-stars.

In a nutshell, hydrodynamical simulations are not yet fully realistic, but they provide a good approximation of reality for small clusters and allow exploration of early dynamical processes.

### 1.4.2 Artificial substructure

There is a persitent difficulty to bridge over self-consistently from the star formation phase, to the equilibrium configuration of bound clusters. Hydrodynamical calculations of star forming regions evolve for up to a few  $\times 10^5$  years, when a stable configuration would require several  $\times 10^6$  years at typical cluster densities of  $10^4$  to  $10^5$  stars per cubic parsec. A way to overcome this issue is to switch to purely gravitational N-body simulations once the stars formed and most



of the gas has been either accreted or expelled. It is computationally less expensive and allows for longer integration of larger systems.

It is then essential to obtain a good model of the stars phase-space distribution at the end of a hydrodynamical simulation. While King and Plummer model have a known distribution one can sample from, no such thing exist for the clumps and filamentary structure of the newborn stellar objects in a star-forming regions. Several methods have been explored to solve this.

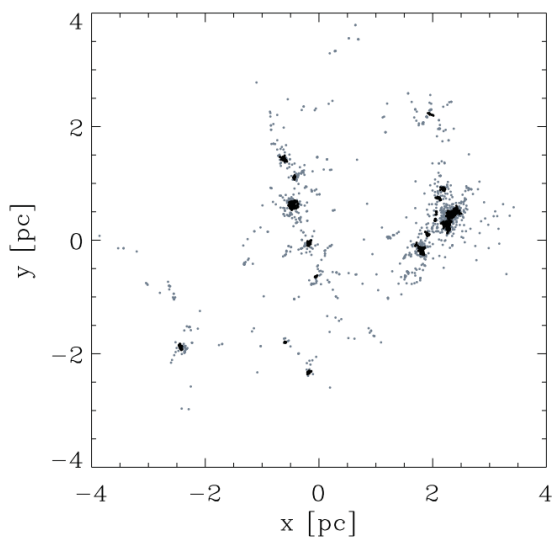
**Sink particle distribution** is the most straightforward solution. [Moeckel & Bate \(2010\)](#) took the distribution of sink particles formed in the hydrodynamical simulation by [Bate \(2009\)](#) and directly converted it as a stellar distribution, preserving the masses, positions and velocities of the "stellar seeds". This is probably the best initial conditions for nbody simulations of young clusters that can be achieved, at the cost of speed, sampling and size. The initial hydrodynamical simulation took months to complete, making it hard to run it again and impossible to run it multiple times to obtain a good statistical sampling of the model. The size of the cluster achieved cannot exceeds 1000 stars given the current state of hydrodynamical simulations.

**Stellar spawning from hydrodynamics** is a variant of the previous method. [Fujii & Portegies Zwart \(2016\)](#) started from hydrodynamical simulations of massive molecular clouds and stopped the integration once the main structures had formed but before local gravitational collapse had set in. Stars were then spawned in space following the distribution of gas. This enables larger clusters and quicker initial conditions of structures. However, the velocity distribution of these new stars is artificial, as it can at best inherit the gas velocity, without including the impact of the early collisional evolution that occurs between protostars in the clumps.

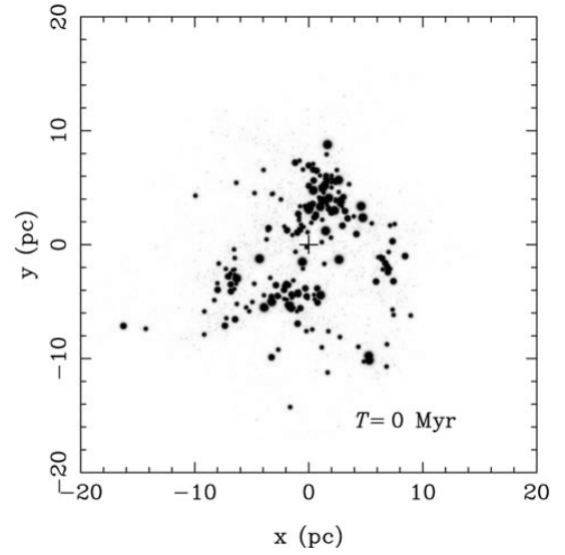
**Scattered Plummer spheres** is an analytic answer to the substructure problem. [McMillan, Vesperini & Portegies Zwart \(2007\)](#) created a clumpy model for a young star cluster by spawning several Plummer spheres randomly in space. This is almost immediate and is a good approximation. The authors obtained interesting results on the inheritance of mass segregation during mergers. However, clumps within a young star clusters have no reason to follow a Plummer profile, this places a constraint on the clumps internal dynamics which bias the dynamical evolution.

**Fractal models** were introduced by [Goodwin & Whitworth \(2004\)](#) and has been used in numerous studies ever since, e.g. [Allison et al. \(2009\)](#); [Kouwenhoven et al. \(2010\)](#); [Parker & Wright \(2016\)](#). The idea is to grow a 3D pseudo-fractal tree with probabilistic branching, down to a given level, turning the final leaves into stars. The method is fast and the result is spatially realistic, fitting the observation that finds a fractal structure in the molecular clouds and star forming regions. However, the velocity distribution is artificial, drawn from successive gaussians at each levels. The clumps will relax when integration starts, shaking the whole system right off the bat.

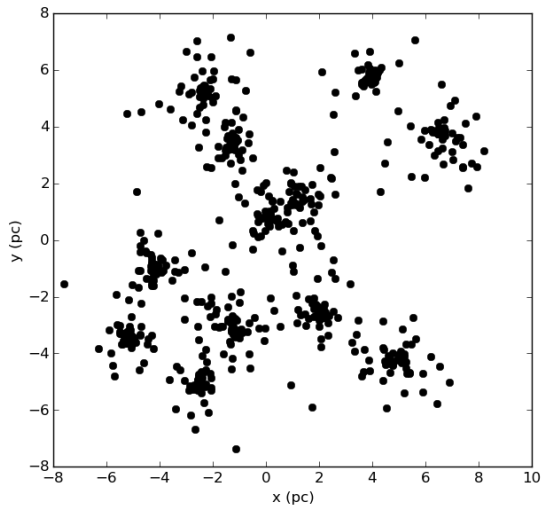
It seems the generation of substructure has to balance realism and computational cost. The most realistic method is too costly, and most of the quicker alternatives are disconnected from the dynamical effect arising from the collisional effects young stars undergo inside a clumpy configuration.



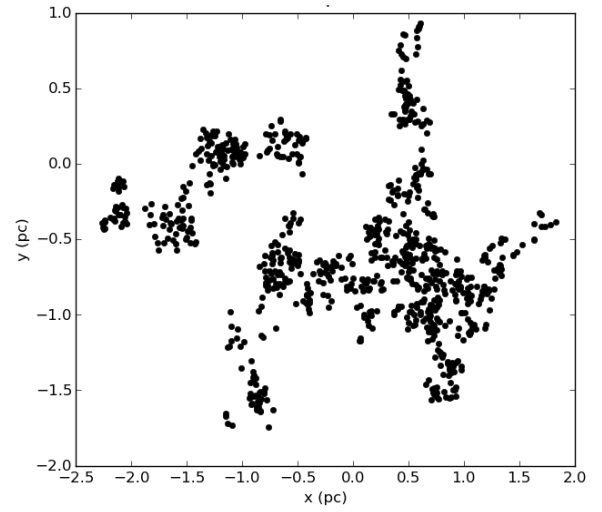
(a) Hydrodynamical output



(b) Stellar spawning



(c) Multiple Plummer



(d) Fractal configuration

Figure 1.9: Representation of four methods to generate substructures. (a) is extracted from (Kruijssen et al., 2012), constructed with data from Bonnell, Bate & Vine (2003), (b) is extracted from Fujii (2015). (c) and (d) were generated for this work.

## 1.5 Binary stars

### 1.5.1 What is a binary star ?

When two massive bodies of mass  $m_1$  and  $m_2$  interact gravitationally, they can have different types of trajectory depending on their total energy:

$$E = E_k + E_p = \frac{1}{2}m_1v_1^2 + \frac{1}{2}m_2v_2^2 - \frac{Gm_1m_2}{\|\mathbf{r}_1 - \mathbf{r}_2\|}. \quad (1.19)$$

If  $E < 0$ , they are bound and locked in a binary system. Such systems are characterised by their semi-major axis  $a$ , their eccentricity  $e$ , their period  $p$ , their total mass  $m_t = m_1 + m_2$ , mass ratio  $q = m_2/m_1$  with  $m_1$  being the primary, more massive than  $m_2$ . Mass, period and semi-major axis are related by Kepler's third law:

$$\frac{Gm_t}{4\pi^2} = \frac{a^3}{p^2}. \quad (1.20)$$

Interestingly, expressed in AU,  $M_\odot$  and years,  $G \simeq 4\pi^2$ , thus the law can be written:

$$\left(\frac{m_t}{1M_\odot}\right) = \left(\frac{p}{1\text{yr}}\right) \left(\frac{a}{1\text{AU}}\right)^3. \quad (1.21)$$

The total energy of the binary can be expressed as a function of  $a$  and  $m_t$ :

$$E = -\frac{Gm_1m_2}{2a} \quad (1.22)$$

### 1.5.2 Why binaries ?

Binary stars are extremely important for a variety of reasons. They can be a reservoir of energy, supporting the core of a cluster against collapse by giving away their internal energy to perturbers, effectively ejecting stars and heating the system, affecting its global evolution and stopping core collapse (e.g. [Heggie & Aarseth 1992](#)).

The properties of binary stars in dense stellar associations in particular may shed light on the discovery of multiple star-formation episodes in rich stellar clusters ([Anderson et al., 2009](#)). For instance, binary stars enhance strong dynamical interactions which in turn may speed-up evolution off the main sequence and so boost enrichment of the ISM through winds (e.g., [Tailo et al. 2015](#)). Tight binaries of short-lived massive stars may evolve to produce exotic stellar remnants including black hole progenitors ([Bacon, Sigurdsson & Davies, 1996](#); [Davies et al., 2009](#)).

Finally, accurate knowledge of binary population in stellar clusters enable good estimation of their dynamical mass, as the integrated velocity dispersion is largely biased by the binaries internal motions, see [Rubenstein & Bailyn \(1997\)](#).

### 1.5.3 Multiplicity fraction

In a stellar population, some fraction of stars will be found in multiple systems: some in binaries and some in higher order hierarchies. A hierarchical triple is a stable 3-body bound system, a binary of which one of the component is a binary itself. The same principle applies to quadruple, quintuple, etc. One of the brightest stars in the night sky, Castor, is a sextuple hierarchical system, with 6 stars in a stable system.

Counting binaries and multiples is not straightforward: do you count triples as two binaries or three stars in a multiple system ? In their SPH simulation paper, [Goodwin, Whitworth & Ward-Thompson \(2004\)](#) discuss several ways to measure the degree of multiplicity among

stars in a system, each of them quantifying different properties, such as companion probability, companion frequency or pairing factor.

Let  $S$  be the number of single stars, and  $B, T$ , and  $Q$  the number of binary-, triple-, and quadruple systems, respectively. The fraction of multiple stars bound in binaries, triples, .. to the total number of multiple plus single stars, is

$$f_m = \frac{B + T + Q}{S + B + T + Q}. \quad (1.23)$$

This last measure is used in seminal observationnal papers (Duquennoy & Mayor, 1991; Raghavan et al., 2010) and is our adopted choice. As pointed out by Hubber & Whitworth (2005),  $f_m$  in Eq. (1.23) has several advantages: 1) it may be restricted to a given mass  $m$ , setting  $S_m$  the number of single stars, and  $B_m, T_m, Q_m$  the multiple stars with a primary of that mass ; 2) the multiplicity fraction is observationally robust: when a binary is being reclassified as a triple, or an even higher order multiple system, the fraction does not change. These definitions may be extended to cover a mass range in a coherent way, by substituting  $m \rightarrow \langle m \rangle$ , the mean value over the range. This is useful mostly when comparing systems with different stellar mass functions.

### 1.5.4 Observed population

The first real complete survey of binary solar-type stars in the field was performed by Duquennoy & Mayor (1991). This seminal paper was updated and completed by Raghavan et al. (2010), who essentially confirmed the main results from the first study. They observed hundreds of F and G main-sequence stars in pairs and derived their binary parameters. The total binary fraction for these stars was found to be  $\sim 53\%$  as binaries are quite common in any stellar population. The authors also derived a period distribution, extending from less than a day to more than a Myr. The distribution was consistently well fitted by a log-normal distribution. The period distribution for F and G stars (as well as K and M stars, see Fischer & Marcy 1992) is:

$$f(\log P) \propto \exp \left[ \frac{-(\log P - \mu_{\log P})^2}{2\sigma_{\log P}^2} \right] \quad (1.24)$$

with the peak value  $\mu_{\log P} = 5.03$ , about 300 years, and the dispersion  $\sigma_{\log P} = 2.28$ , the distribution is shown on fig [TODO].

Raghavan et al. (2010) also compiled several observational studies of binaries with primaries of various spectral types. High mass stars, types O,B,A, (from 30+ down to  $2M_{\odot}$ ) have a high multiplicity fraction, about 75% while lower mass stars such as M-dwarfs only have 10-30% multiplicity. This trend of increasing multiplicity with increasing primary mass is found in many surveys. Binary surveys are easier in the field due to the very large sample and low stellar density. To perform similar studies in young star clusters is much harder due to source crowding and embedded stars. Kouwenhoven et al. (2007) attempted to characterize the birth binary population in the OB association Scorpius OB2. They found a very high multiplicity fraction, consistent with 100%, and a period distribution more consistent with a powerlaw than a log-normal distribution. From this survey and others, it is likely that the binary population in clusters undergoes an erosion through dynamical processing, with the field distribution as an end-result.

### 1.5.5 Simulate binary populations in clusters

As noted earlier, young clusters are born substructured, then undergo dynamical evolution. The rapid, global merging of sub-structures would bring together stars at a different stage of their formation (as in NGC1333, see Foster et al. 2015) while at the same time induce a shift from a

clumpy Taurus-like profile to a more regular one. A simple but important question is how the internal dynamics of such complex configurations may affect the characteristics of a population of binary stars.

Many authors have explored this question through optimised initial conditions (Kroupa & Burkert, 2001; Marks & Kroupa, 2012) or fractal configurations evolved with N-body integrators (Parker, Goodwin & Allison, 2011; Parker & Meyer, 2014). A common feature to all these studies is that the binary fraction drops over time regardless of their components (masses), due e.g. to close star-star encounters or heating from the external galactic tidal field. Parker & Meyer (2014) pointed out that the distribution of semi-major axes  $a$  of the field population is a strong function of the primary’s mass: at fixed  $a$ , low-mass binaries carry less binding energy so the distribution cuts off at shorter separation ( $\sim 20$  AU) compared to that for binaries with a more massive primary ( $\sim 300$  AU). Their study of fractal initial conditions show that gravitational dynamics enhances the dissolution of low-mass systems. This then provides a clue to account for the larger relative fraction of heavy stars in binaries, such as seen in a compilation by Raghavan et al. (2010).

We note that hydrodynamical calculations of star formation have found young heavy stars to be preferentially found in dense clumps (Maschberger et al., 2010). Furthermore, it is not clear yet whether binary populations should be tailored according to the total system mass because of the limited range of  $M \sim 10^2$  to  $\sim 10^3 M_\odot$  of these studies (Kroupa & Burkert, 2001; Parker, Goodwin & Allison, 2011; Parker & Meyer, 2014). Recall that the intensity of the tidal field is a prime agent of binary heating. A trend with mass may be expected on the ground that the drive to equilibrium of more massive systems leads to deeper potential wells (e.g. Aarseth, Lin & Papaloizou 1988; Boily, Athanassoula & Kroupa 2002). A steep potential will give rise to strong tidal fields which may disrupt bound sub-systems (Boily et al., 2004; Renaud, Gieles & Boily, 2011). A definitive assesment of this effect is difficult to reach because the results are a strong function of the system initial mass distribution and kinetic energy content (Boily, Athanassoula & Kroupa, 2002; Caputo, de Vries & Portegies Zwart, 2014).

## 1.6 NBODY6

NBODY6 is the second youngest iteration of the NBODY family, a suite of n-body integrators created by Sverre Aarseth. It can compute the gravitational interaction between up to 128,000 stars in a collisional fashion, meaning there is no softening of the potential, at any scale. This allows for very close binaries to form and remain in the system. To achieve its impressive performances, NBODY6 relies on several optimization technique which have been first developed in the 1960s and 1970s, and improved ever since. Here will be developped five major features of NBODY6, in chronological order of their implementation: Hénon units, block time-step, KS-regularization, Hermite scheme and Ahmad-Cohen neighbour scheme. A full description can be found in Sverre Aarseth's book ([Aarseth, 2003](#)). Inspiration for this section should be credited to the user manual of NBODY6++, written by Emil Khalisi and Rainer Spurzem.

### 1.6.1 Hénon units

NBODY6 uses a set of units specifically invented for the Nbody gravitational problem, the Nbody units, or Hénon units (as prescribed by Douglas Heggie during the MODEST 2014 meeting). These units are based on three relations:

$$G = 1 \tag{1.25}$$

$$M_t = 1 \tag{1.26}$$

$$E = -\frac{1}{4} \tag{1.27}$$

With  $G$  the gravitational constant,  $M_t$  the total mass of the system and  $E$  total energy of the system. For a virialized system, that is a relaxed system in which the virial ratio

$$Q = -\frac{E_k}{E_p} = 0.5 \tag{1.28}$$

it comes that  $E_k = 0.25$  and  $E_p = -0.5$  and, considering the definition of the virial radius

$$R_v = -\frac{GM_t^2}{2E_p} = 1. \tag{1.29}$$

This unit system was designed for virialized systems, but can be used for out of equilibrium systems, as long as they are bound ( $Q < 1$ ), with energy expressions functions of  $Q$

$$E_p = -\frac{1}{4(1-Q)} \tag{1.30}$$

$$E_k = \frac{Q}{4(1-Q)} \tag{1.31}$$

which still fulfills the  $E = -\frac{1}{4}$  condition. In practice, the Hénon mass, radius and velocities are obtained through

$$m_h = \frac{m}{M_t} \tag{1.32}$$

$$r_h = 4(1-Q)|E_p| \cdot r \tag{1.33}$$

$$v_h = \sqrt{\frac{Q}{4(1-Q)E_k}} \cdot v \tag{1.34}$$

which can be used as an input for NBODY6.

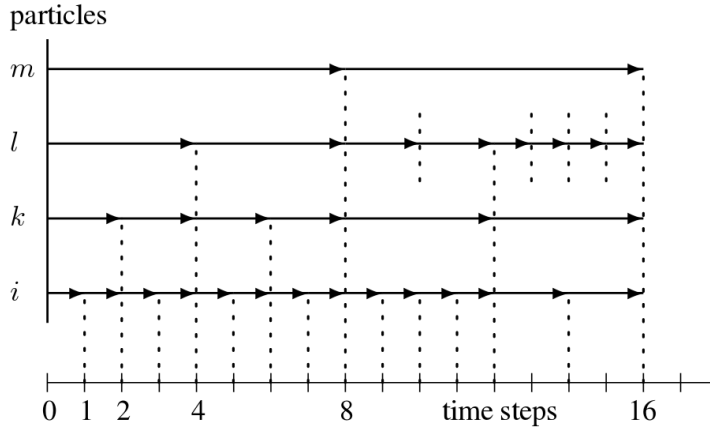


Figure 1.10: Illustration of block time steps on 4 particles. Particles get their positions updated for each arrow symbol, common time steps are shown as vertical dotted lines. Figure from NB6++ User Manual.

### 1.6.2 Block time-step

In the first Nbody simulations, the system was integrated with an universal time-step, determined by the most accelerated star. A star in the outer regions of the cluster with a small velocity did not need to be updated that often. One of the first improvement was the introduction of individual time-step: each star is attributed its own time-step, depending on the force that is applied to it and its derivative:

$$\Delta t_i = \eta \sqrt{\frac{|\mathbf{F}_i| |\mathbf{F}_i^{(2)}| + |\mathbf{F}_i^{(1)}|^2}{|\mathbf{F}_i^{(1)}| |\mathbf{F}_i^{(3)}| + |\mathbf{F}_i^{(2)}|^2}} \quad (1.35)$$

With  $\mathbf{F}_i^{(j)}$  begin the j-th derivative of the force applied to particle i and  $\eta$  a user-defined accuracy parameter. Such a complex formulation is the result of extensive tests and is quite robust for many special cases. Individual time-steps leads to desynchronized particles, hence the need to interpolate the positions of other particles to compute  $\mathbf{F}_i$ , which was achieved through fourth-order polynoms.

To limit the amount of desynchronization, block-time steps were introduced. Instead of having as many time steps as particles, one only allows quantized power of 2 of an initial time step.  $\Delta t_0, \frac{\Delta t_0}{2}, \frac{\Delta t_0}{4}, \frac{\Delta t_0}{2^i}$ . All time steps are then commensurate and regularly fall back on the same time steps, minimizing the amount of interpolation during the force calculations.

### 1.6.3 KS-regularization

Close binaries are extremely problematic in N-body simulations. They require a small time step as both binary components are much more accelerated than any other stars in the system, while the rest of the system is unaffected. Block time-step mitigate this problem, but the binary system still requires a lot of integration for an orbit that is essentially already known. Regularization is an answer to this problem. The essence of regularization is to decouple the integration of a sufficiently isolated sub-system, changing its coordinates to make integration easier, and including perturbations from external bodies. Several regularization scheme exist, NBODY6 implemented the Kustaanheimo-Stiefel method, or KS ([Kustaanheimo & Stiefel, 1965](#)).

Two bodies are candidates for regularization when their impact parameter is lower that the one needed for an orthogonal deviation, wherein their trajectory are deviated of  $90^\circ$ :

$$b_\perp = 2G \frac{m_1 + m_2}{v_\infty^2} \quad (1.36)$$

with  $m_i$  components masses and  $v_\infty$  relative velocity before encounter. This impact parameter can be converted to a time step computed through equation 1.35:

$$dt_{min} = \kappa \frac{\eta}{0.03} \left( \frac{r_{min}^3}{\langle m \rangle} \right)^{\frac{1}{2}}. \quad (1.37)$$

To be actually regularized, two bodies have to have a mutual time step lower than  $dt_{min}$  and fulfill two conditions:

$$\mathbf{R}_r \cdot \mathbf{V}_r > 0.1 \sqrt{G(m_1 + m_2) R_r} \quad (1.38)$$

$$\frac{|\Delta \mathbf{F}_r| \cdot R_r^2}{G(m_1 + m_2)} < 0.25. \quad (1.39)$$

$\mathbf{R}_r$  and  $\mathbf{V}_r$  being the relative velocities and positions of the particles and  $|\Delta \mathbf{F}_r|$  the differential force applied to them, or perturbation. These conditions mean the subsystem is dynamically decoupled from external influence, but not unperturbed. When they are satisfied, the subsystem is regularized: it is replaced by the center of mass in the global system, and computed separately, with a set of changed coordinates. These coordinates are tailored for binary motion and close approach, they are well behaved when  $R_r \rightarrow 0$ . The influence of perturbers is taken into account when necessary. When the perturbation ratio (left hand side of equation 1.39) drops below a certain value, the system is considered isolated and it is not computed anymore, its parameters being stored until the perturbation is strong enough to warrant integration.

Regularisation have been extended to 3 and 4 bodies in hierarchical subsystems. NBODY6 can handle the regularization of a small-n non-hierarchical subsystem following the chain algorithm, see Mikkola & Aarseth (1993).

#### 1.6.4 Hermite integration scheme

On the appropriate time-scales, the accelerations of the particles in a nbody system vary smoothly. It is therefore possible to predict the future acceleration then to correct the prediction, achieving high order integration with limited computational cost. The Hermite integration scheme was first introduced by Makino (1991) and has since been implemented within NBODY6 (Aarseth, 2003).

The first step is to compute the acceleration and its derivative at  $t = t_0$ , for all particles  $i$ :

$$\mathbf{a}_{0,i} = - \sum_{j \neq i} G m_j \frac{\mathbf{R}}{R^3} \quad (1.40)$$

$$\dot{\mathbf{a}}_{0,i} = - \sum_{j \neq i} G m_j \left[ \frac{\mathbf{V}}{R^3} + \frac{3\mathbf{R}(\mathbf{V} \cdot \mathbf{R})}{R^3} \right] \quad (1.41)$$

with  $\mathbf{R} = \mathbf{r}_{0,i} - \mathbf{r}_{0,j}$  and  $\mathbf{V} = \mathbf{v}_{0,i} - \mathbf{v}_{0,j}$ . Using these quantities, it is now possible to predict the positions and velocities at  $t$  through a Taylor serie, again for all particles  $i$ :

$$\mathbf{r}_{p,i}(t) = \mathbf{r}_0 + \mathbf{v}_0(t - t_0) + \mathbf{a}_{0,i} \frac{(t - t_0)^2}{2!} + \dot{\mathbf{a}}_{0,i} \frac{(t - t_0)^3}{3!} \quad (1.42)$$

$$\mathbf{v}_{p,i}(t) = \mathbf{v}_0 + \mathbf{a}_{0,i}(t - t_0) + \dot{\mathbf{a}}_{0,i} \frac{(t - t_0)^2}{2!} \quad (1.43)$$

The predicted accelerations and their derivatives  $\mathbf{a}_{p,i}(t)$ ,  $\dot{\mathbf{a}}_{p,i}(t)$  are computed by injecting  $\mathbf{r}_{p,i}(t)$  and  $\mathbf{v}_{p,i}(t)$  into equations 1.40 and 1.41. The accelerations at  $t$ , of which predicted values have just been computed, can also be obtained through Taylor series:



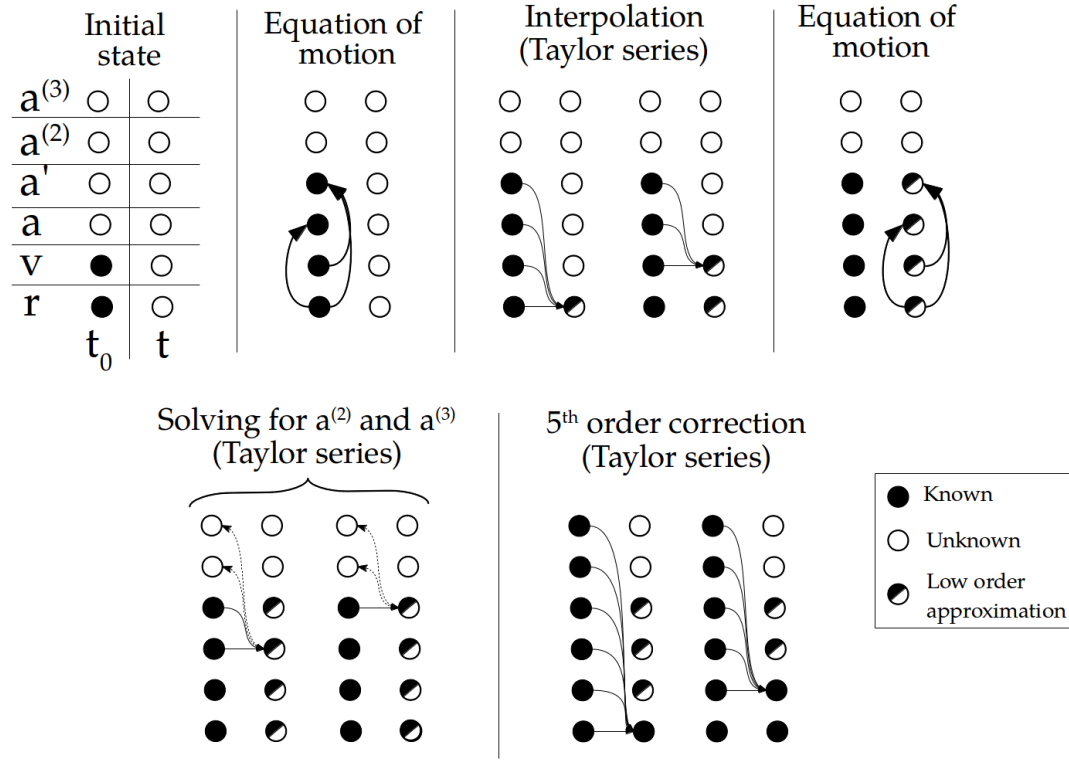


Figure 1.11: Summary of the Hermite scheme starting from known positions and velocities at  $t_0$  to obtain 5th order values at  $t$ .

$$\mathbf{a}_i(t) = \mathbf{a}_{0,i} + \dot{\mathbf{a}}_{0,i}(t - t_0) + \mathbf{a}_{0,i}^{(2)} \frac{(t - t_0)^2}{2!} + \mathbf{a}_{0,i}^{(3)} \frac{(t - t_0)^3}{3!} \quad (1.44)$$

$$\dot{\mathbf{a}}_i(t) = \dot{\mathbf{a}}_{0,i} + \mathbf{a}_{0,i}^{(2)}(t - t_0) + \mathbf{a}_{0,i}^{(3)} \frac{(t - t_0)^2}{2!} \quad (1.45)$$

with  $\mathbf{a}_{0,i}^{(2)}, \mathbf{a}_{0,i}^{(3)}$  the third and fourth derivative of the acceleration at  $t = 0$ . Note that these quantities are unknown for now. To take the derivatives of equation 1.41 would be too computationally expensive. Instead,  $\mathbf{a}_{p,i}(t)$  and  $\dot{\mathbf{a}}_{p,i}(t)$  are injected in the left hand side of equations 1.44 and 1.45 and solved for  $\mathbf{a}_{0,i}^{(2)}$  and  $\mathbf{a}_{0,i}^{(3)}$ . This leads to the expressions:

$$\mathbf{a}_{0,i}^{(3)} = 12 \frac{\mathbf{a}_{0,i} - \mathbf{a}_{p,i}}{(t - t_0)^3} + 6 \frac{\dot{\mathbf{a}}_{0,i} - \dot{\mathbf{a}}_{p,i}}{(t - t_0)^3} \quad (1.46)$$

$$\mathbf{a}_{0,i}^{(2)} = -6 \frac{\mathbf{a}_{0,i} - \mathbf{a}_{p,i}}{(t - t_0)^2} - 2 \frac{2\dot{\mathbf{a}}_{0,i} + \dot{\mathbf{a}}_{p,i}}{t - t_0}. \quad (1.47)$$

The predicted values of positions and velocities are then corrected using the second and third order derivatives of acceleration, yielding fifth order accurate values.

$$\mathbf{r}_{c,i}(t) = \mathbf{r}_{p,i}(t) + \mathbf{a}_{0,i}^{(2)} \frac{(t - t_0)^4}{4!} + \mathbf{a}_{0,i}^{(3)} \frac{(t - t_0)^5}{5!} \quad (1.48)$$

$$\mathbf{v}_{c,i}(t) = \mathbf{v}_{p,i}(t) + \mathbf{a}_{0,i}^{(2)} \frac{(t - t_0)^3}{3!} + \mathbf{a}_{0,i}^{(3)} \frac{(t - t_0)^4}{4!} \quad (1.49)$$

$$(1.50)$$

In a nutshell, the Hermite scheme is a way to obtain 5th order terms with limited cost. The steps are summarised in figure 1.11. First  $r_0^{(2)}$  and  $r_0^{(3)}$  are computed, then used to obtain predictions of  $r_t^{(0)}$  and  $r_t^{(1)}$ , transformed with the equations of motions into predictions of  $r_t^{(3)}$  and  $r_t^{(4)}$ . These last two can be expressed through Taylor series as functions of  $r_0^{(3)}, r_0^{(4)}$  and  $r_0^{(5)}$ , which are solved for these last two terms. The predicted values of  $r_t^{(0)}$  and  $r_t^{(1)}$  are then corrected to the fifth order with  $r_0^{(4)}$  and  $r_0^{(5)}$ .

The error for a single time step scales as  $O(\Delta t^5)$ . The Hermite scheme has shown itself very well suited for the block time step method, as the synchronization of particles limit the amount of prediction to be made, many positions at a given time being already known and computed with maximum accuracy.

### 1.6.5 Ahmad-Cohen neighbour scheme

For a given particle in an nbody system, the influence of direct neighbours changes on shorter timescales than the smooth potential from distant particles. The essence of the Ahmad-Cohen neighbour scheme is to decouple the two for computational efficiency (Ahmad & Cohen, 1973). The acceleration is splitted into two components:

$$\mathbf{a}_i = \mathbf{a}_{i,reg} + \mathbf{a}_{i,irr} \quad (1.51)$$

$\mathbf{a}_{i,irr}$  is the acceleration from particles inside a given "neighbour sphere" around particle  $i$ , while  $\mathbf{a}_{i,reg}$  is the acceleration from all other, more distant, particles. Integration within the neighbours sphere, *irregular* integration, is decoupled from the global, *regular*, integration. Regular time steps, where complete force summation are performed over all particles with eq 1.40, are subdivided into irregular time steps, where regular acceleration is predicted and irregular acceleration is computed through a force summation on the  $N_{i,nb}$  neighbours. The list of neighbours of  $i$  is updated every regular time step and contains the particles within a sphere of radius  $R_{i,s}$  centered on  $i$ . Are also added to the neighbour list are the particles within  $2^{\frac{1}{3}} R_{i,s}$  that satisfy the condition

$$\mathbf{R} \cdot \mathbf{V} < 0.1 \frac{R_s^2}{\Delta T_{reg}} \quad (1.52)$$

with  $\Delta T_{reg}$  the regular time step. This ensures that fast approaching particles are selected before they enter the actual neighbour sphere.  $R_{i,s}$  is determined through local number density contrast and optimisation of the resulting  $N_{i,nb}$ .

When  $N_{nb} \ll N$  for most particles, there is a great performance improvement, without loss of accuracy.

# CHAPTER 2

## The Hubble-Lemaître fragmented model

### 2.1 How to build a Hubble-Lemaître model

#### 2.1.1 Initial state

The first step to obtain a HL-fragmented model is to build an uniform sphere model. The N stars, depending on the required membership, have to be distributed randomly in space inside a certain radius, producing an uniform density. This can be achieved by sampling separately the distance to the center and the angular position of each star, in a method analog as used in [Aarseth, Hénon & Wielen \(1974\)](#) for a Plummer model. The distance to the center should be sampled from the function:

$$f_R(X) = R_0 X^2 \quad (2.1)$$

With  $R_0$  the bounding radius and X a random variable following a uniform probability law between 0 and 1. A direct uniform law for the radius would overpopulate the outer regions. The angles  $\phi$  and  $\theta$ , respectively azimuthal and polar angle in the physics convention, should be sampled from:

$$f_\phi(X_1) = 2\pi X_1 \quad (2.2)$$

$$f_\theta(X_2) = \arccos(X_2) \quad (2.3)$$

With  $X_1$  following a uniform probability law between 0 and 1 and  $X_2$  between -1 and 1. The cartesian coordinates are then found:

$$x = R \sin \theta \cos \phi \quad (2.4)$$

$$y = R \sin \theta \sin \phi \quad (2.5)$$

$$z = R \cos \theta \quad (2.6)$$

$$(2.7)$$

The N particles are then homogeneously distributed in space in a sphere of radius  $R_0$ . The next step is to attribute velocities. Unlike other models like the Plummer model, the velocities are here straightforward. We use the well known velocity field of neighbouring galaxies: velocities are radial from the Milky Way, larger with increasing distances, taking the form:

$$\mathbf{v} = H_0 \mathbf{r}, \quad (2.8)$$

with  $H_0$  being an equivalent of the well-known Hubble parameter. For historical accuracy, I added the name of Georges Lemaître when I named my model. It has now been shown that the astronomical observations of redshifted galaxies and its interpretation as the consequence of an expanding universe predated Hubble's paper (Hubble, 1929). Georges Lemaître had published his conclusion on an expanding universe two years earlier (Lemaître, 1927). The account of this can be found in Kragh & Smith (2003); van den Bergh (2011) and Freeman et al. (2015).

An appropriate  $H_0$  to obtain a fragmented subvirial model has to be inferior to 1.4 (see next section). The model obtained from this is then evolved through a nbody integrator, which in my case is NBODY6.

### 2.1.2 Fragmentation

The cluster expands, driven by the initial Hubble-Lemaître velocity field. During this expansion, poissonian fluctuation in density from the uniform model starts to grow: the part of the cluster with more mass initially attract more stars, forming clumps, clumps merge, spontaneously building substructure. These clumps will be analyzed in another section. If  $H_0$  is well chosen, the expansion stops at some point, the apex, at which the initial kinetic energy has been spent and converted to potential energy: the cluster is now larger, substructured and subvirial, about to collapse. The apex time  $t_a$  of the end of the expansion and the critical value of  $H_0$  can be derived from Newton's second law applied to an expanding spherical shell of matter.

We start from a uniform sphere of radius  $R_0$ , total mass  $M$ . We consider spherical shells as mass elements, situated at distance  $r$  from the origin. As previously said, they are attributed a radial velocity following (for the shell at  $r = R_0$ )  $\vec{v}_0 = H_0 \vec{R}_0 = H_0 R_0 \vec{u}_r$ . We want to follow the radial motion of the last shell of mass  $m$ , situated at  $R$  from the origin. Newton's second law gives:

$$m \frac{dv}{dt} = -\frac{GMm}{R^2} \quad (2.9)$$

By multiplying on both sides by  $v$  and integrating between a given time and  $t = 0$ , one finds:

$$v^2(t) - v_0^2 = 2GM \left( \frac{1}{R} - \frac{1}{R_0} \right) \quad (2.10)$$

Which becomes, by taking  $\nu = v/v_0$ ,  $x = R/R_0$  and  $E_* = \frac{2GM}{R_0 v_0^2}$ , which is a dimensionless measure of the total energy of the system:

$$\nu^2 = 1 + E_* \left( \frac{1}{x} - 1 \right). \quad (2.11)$$

The evolution of the system has 3 outcomes, depending on the value of  $E_*$ :

- $E_* < 1$  The velocity is always strictly positive as the system expands ( $x \rightarrow \infty$ ). The system is unbound.
- $E_* = 1$  The velocity approaches zero as the system expands. The expansion "stops at an infinite radius". The system is marginally bound.
- $E_* > 1$  The velocity reaches zero for a finite radius, the system is bound and will collapses back on itself once the expansion stops.

Using Hénon units,  $G = 1$  and  $M = 1$ , and we choose  $R_0=1$ . Which gives a critical value  $E_*$  to have a bound system:  $E_* = \frac{2}{H_0^2} < 1$ . This means to have a bound system, which stops

expanding at some point, one must have  $H_0 < \sqrt{2}$ . We only consider in the following the case in which  $E_* < 1$ . We have the expression

$$\nu = \sqrt{1 + E_* \left( \frac{1}{x} - 1 \right)} \quad (2.12)$$

Taking the time derivative gives:

$$\frac{d\nu}{dt} = -\frac{E_*}{2x^2} \left[ 1 + E_* \left( \frac{1}{x} - 1 \right) \right]^{-\frac{1}{2}} \frac{dx}{dt} \quad (2.13)$$

Combining this with (2.9), one obtains:

$$\frac{dx}{dt} = H_0 \sqrt{1 + E_* \left( \frac{1}{x} - 1 \right)} \quad (2.14)$$

which can be rewritten, using  $\tilde{H}_0 = H_0 \sqrt{E_* - 1}$  and  $x_t = \frac{E_*}{E_* - 1}$

$$\frac{dx}{dt} = \tilde{H}_0 \sqrt{\frac{x_t}{x} - 1} \quad (2.15)$$

$x_a$  being the extent of the maximum expansion as we assumed a bound system. The subscript  $a$  is for apex. If we choose the notation  $u = \frac{x}{x_a}$ :

$$\sqrt{\frac{u}{u-1}} \frac{du}{dt} = \frac{\tilde{H}_0}{x_a} \quad (2.16)$$

We know that  $x$  varies from 1 to  $x_a$ , thus  $u$  varies from  $1/x_a$  to 1. We can then make the change of variable  $u = \sin^2 \theta$  and separate the variables:

$$\sqrt{\frac{\sin^2 \theta}{1 - \sin^2 \theta}} 2 \sin \theta \cos \theta d\theta = \frac{\tilde{H}_0}{x_a} dt \quad (2.17)$$

which becomes after simplifications:

$$[1 - \cos(2\theta)] d\theta = \frac{\tilde{H}_0}{x_a} dt. \quad (2.18)$$

We now integrate the expression from  $t = 0$  to  $t$ , the time at which the expansions stops and  $x$  reaches  $x_a$  (wich implies  $u_a = 1$  and  $\theta_a = \pi/2$ ):

$$\int_{\theta_0}^{\pi/2} [1 - \cos(2\theta)] d\theta = \int_0^t \frac{\tilde{H}_0}{x_a} dt \quad (2.19)$$

$$\frac{\pi}{2} - \theta_0 + \frac{\sin(2\theta_0)}{2} = \frac{\tilde{H}_0}{x_a} t \quad (2.20)$$

$$\pi - 2\theta_0 + \frac{2}{\sqrt{x_a}} \sqrt{1 - \frac{1}{x_a}} = 2 \frac{\tilde{H}_0}{x_a} t \quad (2.21)$$

which boils down to the expression of the time at which the expansion stops:

$$t_a = \frac{E_* \left( \frac{\pi}{2} - \theta_0 \right) + \sqrt{E_* - 1}}{H_0 (E_* - 1)^{-\frac{3}{2}}}. \quad (2.22)$$

Recalling the quantities:

$$E_* = \frac{2GM}{R_0 v_0^2}; \quad x_a = \frac{E_*}{E_* - 1}; \quad \theta_0 = \sin^{-1} \left( \frac{1}{\sqrt{x_a}} \right) \quad (2.23)$$

See figure 2.1 for the value of  $t_a$  as a function of  $H_0$

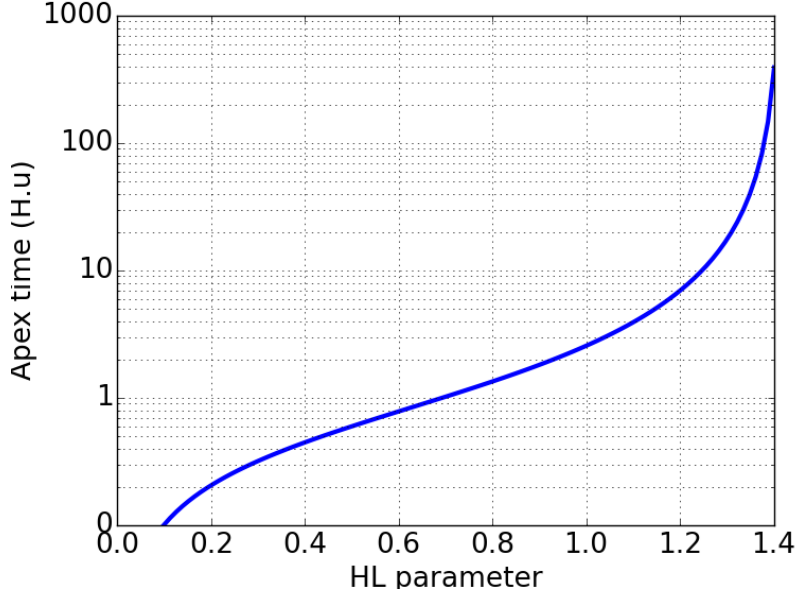


Figure 2.1: Theoretical values of the apex time, at which the system stops expanding, as a function of initial HL parameter, which tunes the strength of the initial expansion.

## 2.2 Perturbation theory

## 2.3 Analysis of the fragmented system

### 2.3.1 Clump finding algorithm

The study of substructures requires an efficient clump-identification algorithm (or, *halo-finding* in cosmology). By clump we mean here a local overdensity of stars. Several methods are commonly used such as the HOP algorithm (Eisenstein & Hut, 1998; Skory et al., 2010) which relies on attributing local densities to each particle and separating the clumps through density thresholds. The HOP algorithm is very robust on large cosmological data sets. However, our calculations have comparatively coarse statistics and noisy density fields. This issue, coupled with the large number of free parameters of the HOP algorithm, makes the method less appealing. Instead

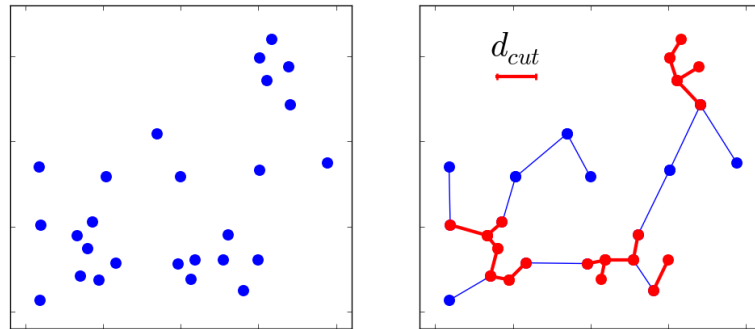


Figure 2.2: Illustration of a Minimum Spanning Tree and its use to isolate subgroups, using a cutting length  $d_{cut}$ .

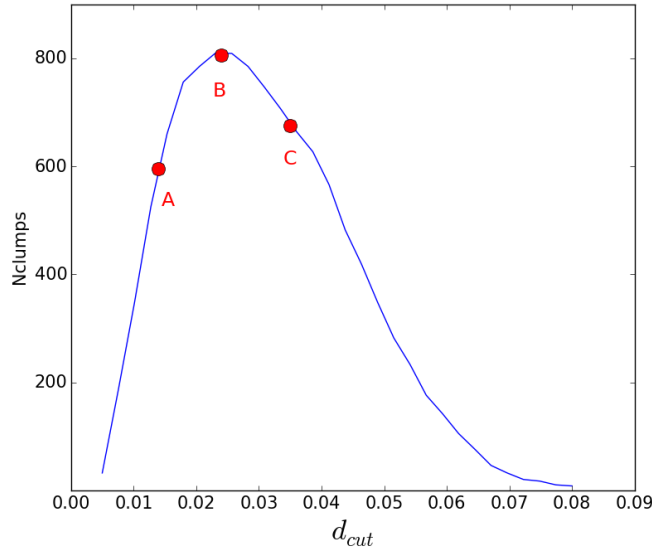


Figure 2.3

we follow [Maschberger et al. \(2010\)](#) who adapted the minimum spanning tree (MST ; see e.g. [Allison et al. 2009](#); [Olczak, Spurzem & Henning 2011](#)) technique to the detection of clumps. A spanning tree is a set of edges connecting a group of particles but without closed loops ; the MST seeks to minimise the total length of the edges. One may then construct the MST for the whole system, and then delete all edges larger than a chosen cutting length,  $d_{cut}$ . The sub-sets that are still connected are labeled as clumps. This process is illustrated in Fig 2.2. In practice a minimum sub-set size  $N_d$  is also chosen so as to avoid many small-N subgroups : experience led us to choose  $N_d = 12$  for the minimum number of stars per clump.

With  $N_d$  fixed, the length  $d_{cut}$  is then the only free parameter left. There is some freedom in choosing an appropriate value. [Maschberger et al. \(2010\)](#) fixed the value of  $d_{cut}$  by visual inspection of clumps. We instead identified clumps in a fragmented system for a range of values for  $d_{cut}$  and settled for the value which optimised the number of identifications. This is shown on Fig. ?? for an  $N = 80k$  fully-fragmented Hubble model. For small  $d_{cut}$ 's, the number of detected clumps at first increases rapidly. The rise is due to the length  $d_{cut}$  initially being small compared with the typical volume spawned by  $N_d$  or more nearest-neighbours. Beyond a certain value, a transition to another regime occurs, whereby the algorithm starts to connect previously separated clumps, counting them as one. The number of clumps thereafter begins to decrease. The value  $d_{cut} \approx 0.025$  H.u optimises the outcome of the clump-search. This is a generic feature of the MST algorithm and we have adopted the same strategy throughout, adapting the value of  $d_{cut}$  to the number  $N$  of stars used.

On Fig. 2.4, a sub-set of the model is shown where we have identified stars that belong to clumps with filled symbols. The three panels on that figure are each for a different value of  $d_{cut}$ , increasing from top to bottom. For the smallest value  $d_{cut}=0.015$  H.u, clumps look somewhat truncated as we are still in the under-sampling regime and only their cores registered as clumps. The second, optimal, value  $d_{cut}=0.025$  H.u produces visually well-isolated clumps. Finally, the third and largest value is so that clumps begin to merge together : this is shown by the unique clump identified in the bottom panel (filled blue squares).

The procedure developed here gives results in agreement with other clump-identification algorithms developed using the MST (see e.g. [Gutermuth et al. 2009](#); [Kirk & Myers 2011](#)).

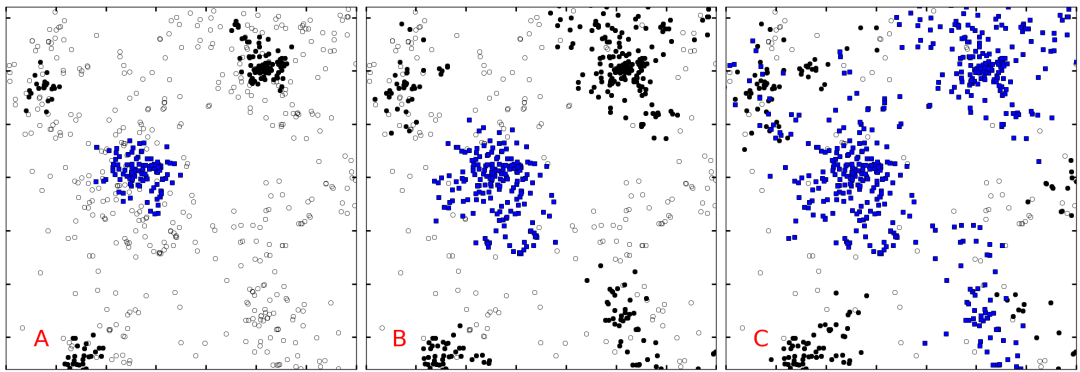


Figure 2.4



# CHAPTER 3

## Dynamical evolution

### 3.1 Bla

The Hubble expansion comes to a halt at a time  $\tau$  when  $\theta(\tau) = \pi/2$  in Eq. (2.8). The system as a whole is then in a sub-virial state. We wish to explore briefly the violent relaxation that follows and the equilibrium that ensues. In the present section, simulations will use the fully fragmented state of Hubble models as initial conditions for the subsequent dynamical evolution. Observationnal clues point to collapsing and violently relaxing clusters. For example, ? find IC348, a young (2-6 Myr) cluster, to be both super-virial and with a convergent velocity field, consistent with infalling motion. Dry collapse with no gas is an idealized situation: clearly if there was residual gas between the clumps and it was evacuated through stellar feedback, both the clump merger rate and the depth of the potential achieved during relaxation would be affected. As a limiting case, rapid gas removal may lead to total dissolution (see for instance ? and ?). In the current situation, all clumps will merge.

The numerical integration were done once more with the Nbody6 integrator with the same computational units. For comparison purposes, we also performed simulations of cold uniform sphere, a configuration which has been extensively used in the past (e.g.,?????) and one that minimises the level of fragmentation and mass segregation in the on-set of collapse. Table 3.1 lists the simulations performed. We focus here on models with a mass function from  $0.35M_{\odot}$  to  $20M_{\odot}$  and 15000 stars, a compromise value for rich open clusters that should allow us to identify clearly collisional effects and trends with time, and ease comparison with the recent study by Caputo et al. (2014) where most calculations are performed with that sampling. We let both Hubble-fragmented- and uniform sphere evolve up to 40 H.u.

#### 3.1.1 Scaling to physical units

Before discussing the results, it is useful to translate the units of computation to physical scales. This is important if we want to discuss the state of the systems using one and the same physical

Table 3.1: Summary of collapse simulations and their characteristics. These simulations started from a subvirial state: cold uniform sphere or fully fragmented Hubble model; each were evolved up to  $t = 40$  H.u

Name	N	Mass range	Model
Rh100	15000	[0.3 - 100]	Hubble
Rh20	15000	[0.35- 20 ]	Hubble
Ru100	15000	[0.3 - 100]	Uniform
Ru20	15000	[0.35- 20 ]	Uniform

Table 3.2: Number of initially ejected stars in two collapse calculations

Run	Ejected stars	Ejected mass
Ru20	4227	27%
Rh20	1932	12%

time, such that the hypothesis of no stellar evolution holds good. This complicates the analysis, because all the time-scales defined in §3.1 are based on the hypothesis of equilibrium, and we start-off out of equilibrium. To make things clearer, let us resize the configurations so that the half-mass radius  $r_h = 1$  pc initially, with a total system mass of  $M = 15 \times 10^3 M_\odot$  for a volume density  $\rho = M/(8\pi/3r_h^3) \simeq 10^3 M_\odot/\text{pc}^3$ , well within values typically inferred from observations. We then compute a free-fall time for the uniform-density model of  $t_{ff} = \pi/2 (r_h^3/GM)^{1/2} \approx (\pi/24)^{1/2} \times 10^5$  years ; the *initial* crossing time would then be  $t_{cr} = 2r_h/\sigma_{1d} = 4\sqrt{6}/\pi t_{ff}$  where we invoked the virial theorem to compute  $\sigma_{1d}^2 = 1/3 \times GM/2/r_h$ . (The crossing time is larger than  $t_{ff}$  because all the mass goes into the origin during free-fall.) In practice the more useful crossing time has to be computed from the equilibrium state achieved. If we once more invoke the virial theorem and note that at constant mass and energy the equilibrium state would reach a size  $r_h^{eq} \approx r_h^{(0)}/2$  or half the initial radius, then one computes  $t_{cr}^{eq} \approx t_{cr}^{(0)}/2\sqrt{2} = 2\sqrt{3}/\pi t_{ff} \approx 1.10 t_{ff}$ . Direct computation of the problem of a collapsing sphere give  $t_{ff} \approx 1.36$  H.u. We therefore use the conversion factor

$$\frac{t}{10^5 \text{ years}} = (4/3)/(\pi/24)^{1/2} \simeq 3.7 t_{Henon}.$$

The equilibrium crossing time is then  $t_{cr}^{eq} = 1.1 t_{ff} = 3/2 t_{Henon} \approx 0.4 \times 10^5$  years. The time-conversion factor adopted is conservative and does not factor in the stars that may escape during virialisation. Thus by running up to 40 H.u we ensure that the systems evolve for at least 25 crossing times and  $\sim 10^6$  years, short before the lifetime of massive stars. With  $N = 15000$  and a mass range of  $m_{max}/\langle m \rangle = 20$  we find from (??) and (??) a two-body relaxation time of  $t_{rel} \approx 80 t_{cr}$  (120  $t_{Henon}$ , or 3 Myrs) and mass-segregation timescale of  $t_{ms} \approx 4 t_{cr}$  (6  $t_{Henon}$ , or  $1.6 \times 10^5$  years).

### 3.1.2 Collapse and virialisation

The constant diffusion of kinetic energy by two-body interaction means that no stellar system ever reaches a steady equilibrium. However we can contrast the time-evolution of two configurations and draw conclusions about their observable properties.

With this in mind we turn to Fig. ?? in which we show the evolution of the half-mass radius for the cold uniform model (labeled Ru20 ; thick red curve), and the Hubble model (labeled Rh20 ; thin blue curve). Both systems have the same bounding radius initially, contract to a small radius when  $t \simeq 1.4$  units and then rebound at time  $t \simeq 2$  units. When all the stars are included in the calculation for  $r_h$ , we find that the radius increases at near-constant speed after the collapse. That trend does not appear to be slowing down which indicates that a fraction of the stars are escaping. The first batch of escapers is driven by the violent relaxation, however the trend continues beyond  $t = 10$  units, corresponding to  $t > t_{ms}$  which implies two-body scattering and effective energy exchange between the stars. Note how the uniform model has a much deeper collapse and rebounds much more violently, shedding a fraction twice as large of its stars (Table 3.2). The half-mass radius  $r_h$  increases steadily in both models, from the bounce at  $t \approx 2$ , until the end of the simulation (values in H.u):

$$\begin{array}{llll} r_h \text{ Uniform} & 0.11 & \rightarrow & 0.63 \quad (\times 5); \\ r_h \text{ Hubble} & 0.34 & \rightarrow & 0.49 \quad (\times 1.4). \end{array}$$

Clearly the gentler collapse of the fragmented model has led to a more extended post-collapse configuration and reduced two-body evolution. Observe how the uniform model Ru20 is ejecting

more stars than the Hubble model : if we repeat the calculation for the Hubble run Rh20 but now include only the bound stars<sup>1</sup>, the curve of  $r_h$  obtained and shown as dash is shifted down but keeps essentially the same slope  $\approx 0.004$ . By contrast, the calculation for the bound stars of run Ru20 yields a much shallower slope than for the whole system: the slope drops from 0.015 to about 0.007. Irrespective of how the half-mass radius is calculated, the conclusion remains the same and agrees overall with the remark by ? that boosting the kinetic energy of the collapsing initial configuration softens the collapse ; this was shown in a different context by ? and confirms these older findings. Here, the fragmented model has finite kinetic energy due to the clumps' internal motion. The important new feature brought by the fragmented initial conditions is that the *mass profile* of the virialised configuration evolves much less over time in comparison.

At the bounce, the half-mass radius of the Hubble model is  $\approx 4$  times larger than that of the of the initially uniform sphere at rest (Fig. 10). The half-mass radii overlap at time  $t \approx 15 H.u.$  (solid curves) or  $t \approx 50 H.u.$  (dashed curves). Is the same trend applicable to all Lagrangian radii? To answer this question we plot on Fig. 11 the ten-percentile mass radii for the two models. The results are displayed for the two situations including all the stars (top row) or bound stars only (middle row). It is striking that the curves show very little evolution at all mass fractions for the case of the Hubble model (see right-hand panels on the figure), whereas all mass shells either contract or expand in time for the uniform one. We have noted how this model undergoes two-body relaxation on a timescale of  $t \approx 10 H.u.$ : the innermost 10% mass shell shows an indication of *core-collapse* at  $t \simeq 5 H.u.$ . We note here that the two sets of curves reach very similar values at the end of the calculations ( $t = 40 H.u.$ ). A key difference between the two models, therefore, is that the final configuration of the Hubble model is almost identical to what it was at the bounce ; the same simply does not hold in the case of a uniform-density collapse. Furthermore, the Hubble calculation shows no hint of two-body relaxation or core-collapse. This raises the possibility that the system properties in the final configuration remain better correlated with those at the on-set of (global) collapse (we return to this point in §7).

? and ? noted how a finite amount of kinetic energy in the *initial* configuration alters the depth of the bounce during collapse. The ratio of half-mass radius at the bounce, to its initial value, is then  $r_h/r_h(0) \simeq Q_o + N^{-1/3}$ , where  $Q_o$  is the virial ratio of the initial configuration (see Fig. 5 of Caputo et al. 2014). We computed the kinetic energy of the Hubble configuraiton and found that the internal motion of the clumps means that  $Q_o(Hubble) \simeq 0.02$  for a Salpeter mass function with upper truncation value of  $20M_\odot$ . With  $N = 15k$  stars, the ratio  $r_h/r_h(0) \simeq 0.041$  when  $Q_o = 0$  shifts to  $r_h/r_h(0) \simeq 0.061$  when  $Q_o = 0.02$ , or a factor close to  $3/2$ . To account for the difference in kinetic energy of the initial configurations, we may therefore rescale the uniform model such that positions are  $\times 3/2$  and the time unit is  $\times (3/2)^{3/2} \simeq 1.84$ . The new configuration would evolve in time in exactly the same way after mapping positions and time to their rescaled values. The result is shown as the bottom row on Fig. 11. Note that we have blown up the vertical axis to ease comparison between uniform- and Hubble models with bound stars only included. The rescaled uniform model is now slightly more extended than before, but overall the final two configurations (at  $t = 40 H.u.$ ) are as close as before rescaling. This demonstrates that the outcome of the uniform collapse and its comparison with the Hubble model is not sensitive to a small amount of initial kinetic energy. We note that while the ratio  $Q_o$  is a free parameter in many setups for collapse calculations, that parameter is fixed internally in the Hubble approach.

### 3.2 Global mass segregation

To investigate the state of mass segregation in our models, we follow the analysis of Caputo, de Vries & Portegies Zwart (2014). The masses are sorted by decreasing values, then subdivided into ten equal-mass bins. This means that the first bin contains the most massive stars. The

<sup>1</sup>See Appendix A for details of the selection procedure.

number of stars in each bin increases as we shift to the following bins, since their mean mass decreases, and so on until we have binned all the stars. The half-mass radius  $r_h$  computed for each bin is then plotted as function of time. In this way the mass segregation unfolds over time: if the stars were not segregated by mass, all radii  $r_h$  would overlap. If two sub-populations share the same spatial distribution, their respective  $r_h$  will overlap.

Figure ?? graphs the results for initially uniform-density- and fragmented Hubble models. The layout of the figure is the same as for Fig. 11. The violent relaxation phase leads to mass loss for both models and the much more rapid expansion of the half-mass radii of low-mass stars is an indication that most escapers have a lower value of mass. Fig. ??(c) and (d) graphs  $r_h$  for the bound stars of each sub-population. Clearly the initially uniform-density model is more compact early on, but note how the heavy stars sink rapidly to the centre, more so than for the case of the Hubble model. The spread of half-mass radii increases with time for both models, however two-body relaxation in the uniform-collapse calculation is much stronger, so that by the end of the simulations the half-mass radii of the low-mass stars of the respective models are essentially identical. Since the low-mass stars carry the bulk of the mass, that means that the two models achieve the same or similar mean surface density by the end of the run. At that time, the heavy stars in the uniform-collapse calculation are clearly more concentrated than in the Hubble run (compare the radii out to  $\sim 40\%$  most massive stars). A direct consequence of this is that the *color* gradients of the core region of a cluster are much reduced when the assembly history proceeds hierarchically, in comparison with the monolithic collapse. It will be interesting and possibly important in future to compare such models with actual data for young clusters.

Another interesting remark is that the kinematics of the stars within the *system* half-mass radius is much different between the two models. For the Hubble calculation, the system half-mass radius,  $\approx 0.43$  H.u., at  $t = 40$  (cf. Fig. 11[d]) coincides with the half-mass radius of the 30 – 40% bin stellar sub-population. All bins up to that range show little or no time-evolution, around the end of the run, which we interpret as efficient retention of these stars by the relaxed cluster. In the case of the uniform-collapse run, the system half-mass radius reaches  $\approx 0.33$  H.u., which is significantly larger than the radius for the 30 – 40% stellar sub-population. For that model, only the bins 0 – 10% and 10 – 20% are flat, and all the others increase almost linearly with time. Thus a fair fraction of bright stars deep in the cluster show systematic *outward streaming* motion, along with low-mass ones. This brings up the possibility to measure this signature motion through relatively bright stars, originating well inside the cluster half-mass radius. Recall that only post-bounce bound stars were selected to compute  $r_h$  on Fig. ??(c) and (d); the expansion is therefore not driven by chance events (e.g., Fig. ??[a]), but rather through two-body relaxation. On the down side the bright tracers would be short-lived, and this may prove a strong constraint for observational detection.

Given the early dynamical evolution associated with substructured stellar clusters, some observed dense objects may yet be out of equilibrium (see §??). We wish to investigate the out-of-equilibrium state of our models just after the collapse. To ease the comparison between the two systems, the same rescaling procedure as for Fig ?? was applied to the uniform model, only this time the scaling was chosen so that the two clusters have comparable densities after the bounce. Lengths were multiplied by 4; the time-axis is then scaled up by a factor  $(4)^{3/2} = 8$ . The result can be seen in panel (e); panel (f) shows a smoothed and zoomed in Hubble model for comparison.

We compare the values of the different half-mass radii of the various population before the dynamical mass segregation sets in. This process is clearly visible as the drop of the half-mass radius of the most massive stars during the evolution. We are interested in the segregation which originates from the collapse and is present before this dynamical evolution. Table 3.3 sums up the values of the half-mass radii taken at  $t \sim 5$  for both models, both corresponding to the same unevolved post-collapse state (see arrows on panels [e] and [f] on Fig ??). With on the order

Table 3.3: Values of half-mass radii and their ratio to that of the most massive stars. The results are for the rescaled bound uniform model (rescaled Ru20b) and the bound Hubble model (Rh20b), after the collapse, and before dynamical mass segregation sets in.

Uniform (rescaled)	0-10%	10-20%	20-30%	30-40%	40-50%	50-60%	60-70%	70-80%	80-90%	90-100%
Radius	0.20	0.245	0.282	0.273	0.294	0.325	0.326	0.328	0.335	0.342
Ratio	1.0	1.23	1.41	1.37	1.47	1.63	1.63	1.64	1.68	1.70
Hubble	0-10%	10-20%	20-30%	30-40%	40-50%	50-60%	60-70%	70-80%	80-90%	90-100%
Radius	0.18	0.21	0.286	0.293	0.316	0.321	0.333	0.338	0.342	0.345
Ratio	1.00	1.16	1.58	1.63	1.76	1.78	1.85	1.88	1.90	1.91

of  $\sim 100$  stars per bin or more, one estimates roughly a ten-percent standard deviation from random sampling. To measure the *relative* segregation between populations, the table also lists the ratios of each half-mass radius to the one for the most massive stars. Both models appear mass segregated (since these ratios are significantly greater than unity). The Hubble model is more segregated, on the whole, albeit in a different way compared to the uniform model. The segregation in that one is more regular and spreads over more mass bins. In the Hubble model, the segregation is much enhanced for the first two mass bins. Such differences in the degree and nature of segregation can be explained by the clumps structure before the collapse. We showed in §?? the clumps were mass segregated with the most massive members being preferentially located at their center. The low membership and mass of most clumps implies that segregation mostly affects the very top of the stellar mass function. This segregation, predominant among massive stars, is then found in the resulting centrally concentrated system, after the collapse, and visible on Fig. ?. The inheritance of mass segregation was studied by ? for the case of merging Plummer spheres. ? furthermore showed that mass segregation in the system as a whole is enhanced for more filamentary fractal initial condition (lower dimension,  $D$  ; see their Fig. 5). Here our results confirm this observation. Mass segregation is a sensitive function of the initial clumpiness of the system and has immediate bearing on the dynamics of the virialised configuration, since all massive stars are more concentrated in the core.



# CHAPTER 4

## Binary population evolution



---

## 4.1 Shock

The equation 8.76 of [Binney & Tremaine \(2008\)](#) gives us the change of energy per unit mass of a self-gravitating system crossing a dense, planar region, in the context of a cluster crossing the galactic disk:

$$\Delta E_s = \frac{14\pi^2 G^2 \Sigma_d^2 a^2}{3V_z^2} \quad (4.1)$$

with  $\Sigma_d$  the surface density of the disk,  $a$  the semi-major axis of stars orbits in the system and  $V_z$  the incoming vertical velocity of the system on the disk. We apply this to a binary falling on the collapsed center of the system ( $R_c$  being the half-mass radius at the point of deepest collapse), we get:

$$\Sigma_d \simeq R_c \rho_c = R_c \frac{0.5M}{\frac{4}{3}\pi R_c^3} = \frac{3M}{8\pi R_c^2}. \quad (4.2)$$

The incoming velocity of a given binary can be approximated by the free fall velocity from the initial half-mass radius of the system  $R_0$ :

$$V_z^2 = \frac{GM}{R_0} \quad (4.3)$$

Injecting equations 4.2 and 4.3 into the expression 4.1 then multiplying by the mass of the binary gives the total energy change of the binary:

$$\Delta E = \frac{14\pi^2}{3} \left( \frac{3}{8\pi} \right)^2 GM m_{bin} a^2 \frac{R_0}{R_c^4} \quad (4.4)$$

$$= 0.65 \frac{GM m_{bin} a^2}{C^4 R_0^3} \quad (4.5)$$

with  $C = \frac{R_c}{R_0}$  the concentration parameter. To get the ratio of energy change, we divide by the internal energy of the binary:

$$\frac{\Delta E}{E} = \frac{\Delta E}{G m_{bin}^2 / a} \quad (4.6)$$

$$= \frac{0.65}{C^4} \cdot \frac{M}{m_{bin}} \cdot \left( \frac{a}{R_0} \right)^3 \quad (4.7)$$

By making reasonable assumptions such as  $C \propto N^{-\frac{1}{3}}$ ,  $M \propto N$  and  $R_0 \propto N^{\frac{1}{3}}$  as we scale the system to preserve the initial density, it comes:

$$\frac{\Delta E}{E} \propto m_{bin}^{-1} a^3 N^{\frac{4}{3}} \quad (4.8)$$

Meaning that an increase of the number of particles will cause shorter binaries to suffer significant energy change. A factor 10 on membership reaches with axis shorter by a factor  $10^{\frac{4}{9}} \simeq 2.8$ .

# Bibliography

---

# Bibliography

- Aarseth S. J., 1972, in BAAS, Vol. 4, Bulletin of the American Astronomical Society, p. 417
- Aarseth S. J., 2003, Gravitational N-Body Simulations. p. 430
- Aarseth S. J., Hénon M., Wielen R., 1974, A&A, 37, 183
- Aarseth S. J., Hoyle F., 1964, Astrophysica Norvegica, 9, 313
- Aarseth S. J., Lin D. N. C., Papaloizou J. C. B., 1988, ApJ, 324, 288
- Ahmad A., Cohen L., 1973, Journal of Computational Physics, 12, 389
- Allison R. J., Goodwin S. P., Parker R. J., Portegies Zwart S. F., de Grijs R., Kouwenhoven M. B. N., 2009, MNRAS, 395, 1449
- Andersen M., Zinnecker H., Moneti A., McCaughrean M. J., Brandl B., Brandner W., Meylan G., Hunter D., 2009, ApJ, 707, 1347
- Anderson J., Piotto G., King I. R., Bedin L. R., Guhathakurta P., 2009, ApJ, 697, L58
- André P. et al., 2010, A&A, 518, L102
- Bacon D., Sigurdsson S., Davies M. B., 1996, MNRAS, 281, 830
- Barker P., Dear P., Christianson J. R., Westman R. S., 2014, Metascience, 23, 203
- Barnes J., Hut P., 1986, Nature, 324, 446
- Barrow-Green J., 1997, Poincaré and the Three Body Problem, History of mathematics No. vol. 2. American Mathematical Society
- Bastian N., Goodwin S. P., 2006, MNRAS, 369, L9
- Bate M. R., 2009, MNRAS, 392, 590
- Bate M. R., 2012, MNRAS, 419, 3115
- Bate M. R., Bonnell I. A., Bromm V., 2003, MNRAS, 339, 577
- Bate M. R., Burkert A., 1997, MNRAS, 288, 1060
- Bédorf J., Portegies Zwart S., 2012, European Physical Journal Special Topics, 210, 201
- Belorizky D., 1930, Bulletin Astronomique, 6, 417
- Binney J., Tremaine S., 2008, Galactic Dynamics (2nd ed.). Princeton Univ. Press, Princeton, NJ
- Boily C. M., Athanassoula E., Kroupa P., 2002, MNRAS, 332, 971

- 
- Boily C. M., Kroupa P., 2003a, MNRAS, 338, 665
- Boily C. M., Kroupa P., 2003b, MNRAS, 338, 673
- Boily C. M., Nakasato N., Spurzem R., Tsuchiya T., 2004, ApJ, 614, 26
- Bonnell I. A., Bate M. R., Vine S. G., 2003, MNRAS, 343, 413
- Bonnell I. A., Smith R. J., Clark P. C., Bate M. R., 2011, MNRAS, 410, 2339
- Bressert E. et al., 2010, MNRAS, 409, L54
- Cambr sy L., 1999, A&A, 345, 965
- Caputo D. P., de Vries N., Portegies Zwart S., 2014, MNRAS, 445, 674
- Clagett M., 1959, The science of mechanics in the Middle Ages, University of Wisconsin publications in medieval science. University of Wisconsin Press
- Clarke C., 2012, in Astronomical Society of the Pacific Conference Series, Vol. 453, Advances in Computational Astrophysics: Methods, Tools, and Outcome, Capuzzo-Dolcetta R., Limongi M., Tornamb  A., eds., p. 3
- Cohen I. B., Anne Whitman J. B., 1999, The Principia: Mathematical Principles of Natural Philosophy, 1st edn. University of California Press
- Dale J. E., Bonnell I., 2011, MNRAS, 414, 321
- Dale J. E., Ngoumou J., Ercolano B., Bonnell I. A., 2013, MNRAS, 436, 3430
- Davies B., Figer D. F., Kudritzki R.-P., Trombly C., Kouveliotou C., Wachter S., 2009, ApJ, 707, 844
- De Angelis A., Santo C. E., 2015, Journal of Astronomical History and Heritage, 18, 241
- de Wit W. J., Testi L., Palla F., Zinnecker H., 2005, A&A, 437, 247
- Dias W. S., Alessi B. S., Moitinho A., L pine J. R. D., 2002, A&A, 389, 871
- Doppler C., 1842, ber das farbige Licht der Doppelsterne und einiger anderer Gestirne des Himmels. Verlag der Knigl. Bhm.
- D’Souza R., Rix H.-W., 2013, MNRAS, 429, 1887
- Duquennoy A., Mayor M., 1991, A&A, 248, 485
- Ebisuzaki T., Ito T., Makino J., Sugimoto D., 1990, Astronomical Herald, 83, 224
- Eddington A. S., 1916, MNRAS, 76, 572
- Eisenstein D. J., Hut P., 1998, ApJ, 498, 137
- Elmegreen B. G., Falgarone E., 1996, ApJ, 471, 816
- Elsen E., Houston M., Vishal V., Darve E., Hanrahan P., V. P., 2006, "n-body simulation on gpus."
- Evans, II N. J. et al., 2009, ApJS, 181, 321
- Farias J. P., Smith R., Fellhauer M., Goodwin S., Candlish G. N., Bla a M., Dominguez R., 2015, MNRAS, 450, 2451

- 
- Field G. B., Goldsmith D. W., Habing H. J., 1969, in BAAS, Vol. 1, Bulletin of the American Astronomical Society, p. 240
- Fischer D. A., Marcy G. W., 1992, ApJ, 396, 178
- Foster J. B. et al., 2015, ApJ, 799, 136
- Freeman K. C., Block D., Elmegreen B. G., Woolway M., 2015, Lessons from the local group : a conference in honour of David Block and Bruce Elmegreen. Springer
- Frisch U., Bec J., Villone B., 2001, Physica D Nonlinear Phenomena, 152, 620
- Fujii M. S., 2015, PASJ, 67, 59
- Fujii M. S., Portegies Zwart S., 2016, ApJ, 817, 4
- Galileo G., 1610, Sidereus nuncius. Thomas Baglioni
- Garcia M., Herrero A., Castro N., Corral L., Rosenberg A., 2010, A&A, 523, A23
- Goodwin S. P., 1997, MNRAS, 284, 785
- Goodwin S. P., Bastian N., 2006, MNRAS, 373, 752
- Goodwin S. P., Whitworth A. P., 2004, A&A, 413, 929
- Goodwin S. P., Whitworth A. P., Ward-Thompson D., 2004, A&A, 423, 169
- Gutermuth R. A., Megeath S. T., Myers P. C., Allen L. E., Pipher J. L., Fazio G. G., 2009, ApJS, 184, 18
- Gutermuth R. A., Pipher J. L., Megeath S. T., Myers P. C., Allen L. E., Allen T. S., 2011, ApJ, 739, 84
- Harris W. E., 1996, VizieR Online Data Catalog, 7195
- Hartmann L., 2002, ApJ, 578, 914
- Hayashi C., 1961, PASJ, 13
- Heggie D., Hut P., 2003, The Gravitational Million-Body Problem: A Multidisciplinary Approach to Star Cluster Dynamics
- Heggie D. C., Aarseth S. J., 1992, MNRAS, 257, 513
- Hillenbrand L. A., Hartmann L. W., 1998, ApJ, 492, 540
- Holmberg E., 1941, ApJ, 94, 385
- Houghton H. E., 1942, Monthly Notes of the Astronomical Society of South Africa, 1, 107
- Hubber D. A., Whitworth A. P., 2005, A&A, 437, 113
- Hubble E., 1929, Contributions from the Mount Wilson Observatory, vol. 3, pp.23-28, 3, 23
- Ito T., Ebisuzaki T., Makino J., Sugimoto D., 1991, PASJ, 43, 547
- Jeans J. H., 1916, MNRAS, 76, 567
- Kandori R. et al., 2005, AJ, 130, 2166
- King I. R., 1981, QJRAS, 22, 227
-

- 
- Kirk H., Myers P. C., 2011, *ApJ*, 727, 64
- Klessen R. S., Burkert A., 2000, *ApJS*, 128, 287
- Kouwenhoven M. B. N., Brown A. G. A., Portegies Zwart S. F., Kaper L., 2007, *A&A*, 474, 77
- Kouwenhoven M. B. N., Goodwin S. P., Parker R. J., Davies M. B., Malmberg D., Kroupa P., 2010, *MNRAS*, 404, 1835
- Kragh H., Smith R. W., 2003, *History of Science*, 41, 141
- Kramer E., 1982, *The Nature and Growth of Modern Mathematics*, Princeton paperbacks. Princeton University Press
- Kroupa P., Burkert A., 2001, *ApJ*, 555, 945
- Kruijssen J. M. D., Maschberger T., Moeckel N., Clarke C. J., Bastian N., Bonnell I. A., 2012, *MNRAS*, 419, 841
- Kuhn M. A., Feigelson E. D., Getman K. V., Sills A., Bate M. R., Borissova J., 2015, *ApJ*, 812, 131
- Kustaanheimo P., Stiefel E., 1965, *J. Reine Angew. Math*, 218, 204
- Lada C. J., Lada E. A., 2003, *ARA&A*, 41, 57
- Larson R. B., 1969, *MNRAS*, 145, 271
- Lemaître G., 1927, *Annales de la Société Scientifique de Bruxelles*, 47, 49
- Mac Low M.-M., Klessen R. S., 2004, *Rev. Mod. Phys.*, 76, 125
- Makino J., 1991, *ApJ*, 369, 200
- Marks M., Kroupa P., 2012, *A&A*, 543, A8
- Maschberger T., Clarke C. J., 2011, *MNRAS*, 416, 541
- Maschberger T., Clarke C. J., Bonnell I. A., Kroupa P., 2010, *MNRAS*, 404, 1061
- Maury J., 1992, *Newton: Understanding the Cosmos*, New horizons in history series. Thames and Hudson
- McKee C. F., Ostriker E. C., 2007, *ARA&A*, 45, 565
- McMillan S. L. W., Vesperini E., Portegies Zwart S. F., 2007, *ApJ*, 655, L45
- Mikkola S., Aarseth S. J., 1993, *Celestial Mechanics and Dynamical Astronomy*, 57, 439
- Miller G. E., Scalo J. M., 1979, *ApJS*, 41, 513
- Moeckel N., Bate M. R., 2010, *MNRAS*, 404, 721
- Moeckel N., Clarke C. J., 2011, *MNRAS*, 415, 1179
- Myers A. T., Klein R. I., Krumholz M. R., McKee C. F., 2014, *MNRAS*, 439, 3420
- Newton S. I., 1687, *Philosophiae Naturalis Principia Mathematica*, Vol. 1
- Nitadori K., Aarseth S. J., 2012, *MNRAS*, 424, 545
-



- 
- Nyland L., Harris M., Prins J., 2004, "the rapid evaluation of potential fields using programmable graphics hardware."
- Offner S. S. R., Hansen C. E., Krumholz M. R., 2009, *ApJ*, 704, L124
- Olczak C., Spurzem R., Henning T., 2011, *A&A*, 532, A119
- Parker R. J., Goodwin S. P., Allison R. J., 2011, *MNRAS*, 418, 2565
- Parker R. J., Meyer M. R., 2014, *MNRAS*, 442, 3722
- Parker R. J., Wright N. J., 2016, *MNRAS*, 457, 3430
- Pavese F., 2015, ArXiv e-prints
- Pelupessy F. I., Portegies Zwart S., 2012, *MNRAS*, 420, 1503
- Poincaré H., 1906, *Bulletin de la société astronomique de France*, 20, 153
- Portegies Zwart S. F., Belleman R. G., Geldof P. M., 2007, *New A*, 12, 641
- Portegies Zwart S. F., McMillan S. L. W., Gieles M., 2010, *ARA&A*, 48, 431
- Raghavan D. et al., 2010, *ApJS*, 190, 1
- Ramasubramanian K., 1998, *Bulletin of the Astronomical Society of India*, 26, 11
- Reipurth B., 2008, *Handbook of Star Forming Regions*
- Renaud F., Gieles M., Boily C. M., 2011, *MNRAS*, 418, 759
- Rubenstein E. P., Bailyn C. D., 1997, *ApJ*, 474, 701
- Scalo J., Vázquez-Semadeni E., Chappell D., Passot T., 1998, *ApJ*, 504, 835
- Schneider S., Elmegreen B. G., 1979, *ApJS*, 41, 87
- Skory S., Turk M. J., Norman M. L., Coil A. L., 2010, *ApJS*, 191, 43
- Springel V. et al., 2005, *Nature*, 435, 629
- Strömgren E., 1909, *Astronomische Nachrichten*, 182, 181
- Sundman K. F., 1912, *Acta Mathematica*, 36, 105
- Tailo M. et al., 2015, *Nature*, 523, 318
- Terlevich E., 1980, in *IAU Symposium*, Vol. 85, *Star Clusters*, Hesser J. E., ed., p. 165
- Teyssier R., 2002, *A&A*, 385, 337
- Turner J. A., Chapman S. J., Bhattal A. S., Disney M. J., Pongracic H., Whitworth A. P., 1995, *MNRAS*, 277, 705
- Tutukov A. V., 1978, *A&A*, 70, 57
- van Albada T. S., 1968a, *Bull. Astron. Inst. Netherlands*, 20, 57
- van Albada T. S., 1968b, *Bull. Astron. Inst. Netherlands*, 20, 40
- van den Bergh S., 2011, *JRASC*, 105, 197
-

---

von Hoerner S., 1960, ZAp, 50, 184

von Hoerner S., 1963, ZAp, 57

von Hoerner S., 2001, in Astronomical Society of the Pacific Conference Series, Vol. 228, Dynamics of Star Clusters and the Milky Way, Deiters S., Fuchs B., Just A., Spurzem R., Wielen R., eds., p. 11

Wang L., Spurzem R., Aarseth S., Nitadori K., Berczik P., Kouwenhoven M. B. N., Naab T., 2015, MNRAS, 450, 4070

Whitmore B. C. et al., 2010, AJ, 140, 75

Wright N. J., Parker R. J., Goodwin S. P., Drake J. J., 2014, MNRAS, 438, 639

Yoccoz J. C., 2010, La Lettre du Collège de France, 28, 38

# List of Figures

1	Left: Depiction of the Ptolemaic geocentric system, the equant is not shown . Right: Copernicus illustration of his own heliocentric system, from <i>De revolutionibus</i> . . . . .	2
2	The evolution of the number of particles in N-body simulations. Solid line shows the Moore law. The figure was taken from Bédorf & Portegies Zwart (2012). . .	6
1.1	Examples of various types of cluster. White bars at the lower left of each pictures show 1 parsec .The dust present in (a) scatters starlight producing this blue haze. (b) contains one million stars and is the largest known star cluster in the Milky Way. <i>Credits: NASA, ESA, AURA/Caltech; ESO/INAF-VST/OmegaCAM</i> . . .	10
1.2	Examples of various types of cluster. White bars still show 1pc. (a) is surrounded by its primordial nebula while (b) is still inside it, the picture is a composite of visible and infra-red light. <i>Credits: NASA, ESA, F. Paresce;T. Rector(U.Alaska Anchorage), H. Schweiker</i> . . . . .	11
1.3	Radius-Mass Diagram for Milky Way clusters. Blue dots are open clusters, red dots Globular clusters and purple squares show Young Massive Clusters. Dashed lines show constant density within half-mass radius $\rho_h = 3M/8\pi r_{hm}^3$ and dotted lines show constant relaxation time. The plot was taken from the review Portegies Zwart, McMillan & Gieles (2010). . . . .	12
1.4	Comparison of King and Plummer models density as a function of radius, for similar core radiuses. . . . .	16
1.5	Visible light and infrared view of a part of the Orion star forming complex. Horshead nebula is visible on the right, as well as the very bright star Alnitak, part of the Orion belt. NGC 2071 and 2068 are visible on the left. Pink infrared coloring shows radiation from very bright young massive stars forming in the cloud. Colder filaments are visible all around. White on lower right of visible shows 1 parsec. <i>Credits: Digitized Sky Survey; ESA/Herschel/PACS</i> . . . . .	17
1.6	Stages of stellar birth. (a) is just cold molecular gas and contains no central source yet. (b) is more advanced, though hidden in visible light, its central protostar shines in infrared.The protostar in (c) is actively accreting its disk and produces jets. (d) is a pre main-sequence star, free from its envelope and surrounded by primordial gas. (e) is the mature stellar stage: the main sequence. <i>Credits: Kandori et al. (2005); NASA/JPL-Caltech/Evans,N; Burrows,C/HST-NASA; ESA/Hubble &amp; NASA; DSS</i> . . . . .	18
1.7	(a): observational data from the Monoceros R2 star forming region. Protostars are shown as red points and gas density (traced through extinction) is shown in greyscale. The figure was extracted from Gutermuth et al. (2011). (b): hydrodynamical simulation of a star forming region yellow points are star-like sink particles and red levels show gas density. The figure was extracted from Bonnell et al. (2011). . . . .	19

---

1.8	(a): hydrodynamical simulation of wind-induced gas expulsion around a small cluster, the figure was extracted from Dale et al. (2013). (b) virial parameter of stellar clumps in a star forming hydrodynamical simulation, ignoring the potential of the gas to predict their post-expulsion fate. The figure was extracted from Kruijssen et al. (2012). . . . .	20
1.9	Representation of four methods to generate substructures. (a) is extracted from (Kruijssen et al., 2012), constructed with data from Bonnell, Bate & Vine (2003), (b) is extracted from Fujii (2015). (c) and (d) were generated for this work. . . .	22
1.10	Illustration of block time steps on 4 particles. Particles get their positions updated for each arrow symbol, common time steps are shown as vertical dotted lines. Figure from NB6++ User Manual. . . . .	27
1.11	Summary of the Hermite scheme starting from known positions and velocities at $t_0$ to obtain 5th order values at $t$ . . . . .	29
2.1	Theoretical values of the apex time, at which the system stops expanding, as a function of initial HL parameter, which tunes the strength of the initial expansion. . . .	36
2.2	Illustration of a Minimum Spanning Tree and its use to isolate subgroups, using a cutting length $d_{cut}$ . . . . .	37
2.3	. . . . .	38
2.4	. . . . .	39

# List of Tables

3.1	Summary of collapse simulations and their characteristics. These simulations started from a subvirial state: cold uniform sphere or fully fragmented Hubble model; each were evolved up to $t = 40$ H.u . . . . .	41
3.2	Number of initially ejected stars in two collapse calculations . . . . .	42
3.3	Values of half-mass radii and their ratio to that of the most massive stars. The results are for the rescaled bound uniform model (rescaled Ru20b) and the bound Hubble model (Rh20b), after the collapse, and before dynamical mass segregation sets in. . . . .	45